TUTORIAL REVIEW

Check for updates

Tumor-on-a-chip platforms to study cancer–immune system crosstalk in the era of immunotherapy

Stefania Parlato,[a] Giulia Grisanti,[bc] Giorgia Sinibaldi,[b] Giovanna Peruzzi,[c] Carlo Massimo Casciola*[bc] and Lucia Gabriele [iD] *[a]

Immunotherapy is a powerful therapeutic approach able to re-educate the immune system to fight cancer. A key player in this process is the tumor microenvironment (TME), which is a dynamic entity characterized by a complex array of tumor and stromal cells as well as immune cell populations trafficking to the tumor site through the endothelial barrier. Recapitulating these multifaceted dynamics is critical for studying the intimate interactions between cancer and the immune system and to assess the efficacy of emerging immunotherapies, such as immune checkpoint inhibitors (ICIs) and adoptive cell-based products. Microfluidic devices offer a unique technological approach to build tumor-on-a-chip reproducing the multiple layers of complexity of cancer–immune system crosstalk. Here, we seek to review the most important biological and engineering developments of microfluidic platforms for studying cancer–immune system interactions, in both solid and hematological tumors, highlighting the role of the vascular component in immune trafficking. Emphasis is given to image processing and related algorithms for real-time monitoring and quantitative evaluation of the cellular response to microenvironmental dynamic changes. The described approaches represent a valuable tool for preclinical evaluation of immunotherapeutic strategies.

[a] Department of Oncology and Molecular Medicine, Istituto Superiore di Sanità, Viale Regina Elena 299, Rome, Italy. E-mail: stefania.parlato@iss.it, lucia.gabriele@iss.it
[b] Department of Mechanical and Aerospace Engineering, Sapienza University of Rome, Via Eudossiana 18, Rome, Italy. E-mail: carlomassimo.casciola@uniroma1.it
[c] Center for Life Nano Science, Istituto Italiano di Tecnologia, Viale Regina Elena 291, Rome, Italy

1 Introduction

The tumor microenvironment (TME) is a dynamic entity tightly connected with peripheral immune populations trafficking to the tumor site through the endothelial barrier. Recapitulating these complex dynamics is critical for

Stefania Parlato is a senior researcher in the Department of Oncology and Molecular Medicine at ISS, Rome, Italy. The main focus of her research is to study of the role of human dendritic cells (DCs) in empowering the anti-cancer immune response. For 10 years, her work has been focused on the understanding of cancer–immune system crosstalk by means of microfluidic platforms to develop preclinical testing for immune-based anticancer treatments.

Stefania Parlato

Giulia Grisanti is a PhD student at Sapienza University (Rome), in affiliation with the Center for Life Nano Science of Istituto Italiano di Tecnologia. After graduating in Medical Biotechnology, she started a PhD project in Theoretical and Applied Mechanics. Her research is focused on producing biological barriers through microfluidics. She works on the realisation of a blood vessel-on-chip model to study the dynamics of endothelial permeabilisation for cavitation-mediated drug delivery, and on the creation of a tumor–vasculature interface-on-chip for immunotherapy studies. Moreover, she works on the production of giant unilamellar vesicles through microfluidics, aimed at investigating phospholipid bilayer biomechanics.

Giulia Grisanti

studying the intimate interactions between cancer and the immune system, and thus to clarify the steps leading to patients' outcome and develop effective therapeutic strategies. This is particularly crucial when it comes to immunotherapy, where immune cells are the key players to counteract tumor progression, strengthening the need to characterize their interaction with cancer cells.[1] In this light, recreating tumor-on-a-chip is a unique technological approach reproducing *in vivo* systems characterized by multiple layers of complexity, suitable to study immunotherapeutic antitumor activities.[2]

Microfluidic devices offer several advantages for the evaluation of physiological and pathological processes in a well-controlled and reproducible manner by bridging biology, engineering and imaging components.[3]

Although in the last two decades microfluidic devices have found a wealth of applications, only recently have they become a central tool for immunotherapeutic studies. Here, we attempt to convey interdisciplinary and complementary fields, including immunology, oncology, immunotherapy, biotechnology, engineering, microfluidics, image processing and analysis to describe technically rigorous concepts and scientific advances on the exploitation of tumor-on-a-chip for immunotherapy testing. In this spirit, we first review, in section 2, the tightly intertwined components of the TME that novel microfluidic-based strategies necessarily need to

Giorgia Sinibaldi

Giorgia Sinibaldi is a researcher at La Sapienza University of Rome, Department of Mechanical and Aerospace Engineering. She supervises the Microfluidic Laboratory of Prof. Casciola's group. Her expertise is in experimental fluid dynamics, microfluidics and aeroacoustics. She is involved in experimental investigation of two-phase flows, cavitation and bubble dynamics and in the biomedical research line focused on the enhancement of tissue permeability through cavitation. She contributed to the realization of a setup to study cavitation mediated endothelial permeabilization in blood vessel-on-a-chip, also exploited for immunotherapy studies.

Giovanna Peruzzi

Giovanna Peruzzi is Technologist at Istituto Italiano di Tecnologia, Center for Life Nano Science in Rome, Italy. She leads the Flow Cytometry Laboratory supporting the scientific projects of the center and to serve as a facility for outside the institute. Due to her expertise in cell biology and immunology, she is additionally involved in several collaborations. Regarding this topic, she acts as a biological referent of microfluidic projects where her knowledge is applied to the establishment and optimization of protocols for the co-culture of endothelial and tumor cells into microfluidic devices that mimic human microvasculature for drug delivery studies.

Carlo Massimo Casciola

Carlo Massimo Casciola is full professor of Fluid Dynamics at La Sapienza University of Rome, Department of Mechanical and Aerospace Engineering, and Senior Fellow of the Sapienza School for Advanced Studies. He leads a group working on the fluid dynamics of complex flows oriented at fundamental, numerical and experimental modeling. After being awarded the ERC AdG 2013 his research focused on different aspects of cavitation and on developing a demonstrator for cavitation enhanced endothelial layer permeability based on a blood-vessel-on-chip in the context of the ERC PoC Grant 2017, INVICTUS, in vitro cavitation through ultrasound.

Lucia Gabriele

Lucia Gabriele received her PhD in Genetics from University Sapienza, Rome. She did her postdoctoral training at NIH, USA. Since then, she has worked in the field of immunology, leading a research group for more than 20 years. Her studies on IFN signaling in immunity to cancer and infectious diseases have contributed to uncovering key aspects of dendritic cell development and function. She is Head of Tumor Immunology Section (ISS, Rome) and Co-Chair of Vaccine Platform EATRIS-ERIC. Her current interests focus on multi-layered innate immune response characterization, as well as microfluidic device development, in various diseases to improve therapeutic host-targeted strategies.

take into account to generate advanced tools suitable for a proper evaluation of immunotherapy efficacy.[4] By focusing on engineering design for the faithful reproduction of the cancer environment, in section 3 we review the most representative papers in the field, starting from the attempts to basically reproduce the crosstalk between immune and cancer cells ending with the development of more complex microfluidic platforms, including structural elements such as the endothelium. Lastly, in section 4, we discuss how imaging techniques applied to microfluidic devices combined with mathematical modeling approaches represent an optimal tool for real-time monitoring and quantitative evaluation of cellular responses to dynamic microenvironmental changes, also generated by drug treatments. Overall, the comprehensive overview of engineering microfluidic platforms for studies on cancer–immune system crosstalk and their potential exploitation in immunotherapies will strengthen pre-clinical and clinical efforts towards patient-on-a-chip models for personalized medicine, as discussed in the closing section. Importantly, the outline of this review can contribute to enlarging the vision for technological progress as well as caveats in this field favoring the use of nanotechnologies in immunotherapy.

2 The key interactions underpinning cancer–immune cell crosstalk modulated by immunotherapy

The TME is a complex highly heterogeneous entity, comprising a broad range of cells, widely represented by cancer cells, immune populations and cells of mesenchymal origin, including endothelial cells (ECs), all embedded in the surrounding extracellular matrix (ECM), containing soluble factors such as chemokines, cytokines and growth factors[5] (Fig. 1). The ECM has a crucial role in cancer growth. During cancer progression, the ECM undergoes biochemical and biomechanical changes increasing the ECM stiffness which leads cancer cells to modify their mechanical properties, such as cytoplasmic viscoelasticity, and to increase their invasive potential.[6] This landscape defines a spatial organization where tumor–immune cell interactions occur. The tumor structure itself generates local biochemical differences, such as gradients of oxygen with hypoxia in the tumor core, pH and growth factors, capable of shaping tumor features. Therefore, tumors exhibit high expression of invasion and proliferation markers in cancer cells located at tumor periphery and low-grade proliferative markers on core cells, as well as differential access of immune cells to the tumor bed.[7,8] This latter phenomenon is highly influenced by spatial factors, such as blood vessel organization. For instance, a high concentration of lactic acid away from blood vessels, due to reduced oxygen availability leading to increased anaerobic glycolysis, is detrimental to immune cells, such as macrophages, which result in their absence in these sites.[9] In

general, variations of blood flow within tumors, both spatially and temporally, lead to large disparity in resource concentration, thus favoring spatial clustering of different cell populations within the tumor mass.[10] Accordingly, angiogenesis is an early event of tumor development. The shortage of oxygen and nutrients within the inner tumor mass stimulates the expression of angiogenic soluble factors, driving continuous formation of new aberrant blood vessels, a phenomenon known as angiogenic switch. The most relevant factors include vascular endothelial growth factor (VEGF) family members and angiopoietin (ANGPT) 2 as well as proangiogenic chemokines and chemokine-receptors, especially CXCL-12 and CXCR-4[11] (see Fig. 1). In this context, the functionality of the endothelial vessel becomes impaired in terms of permeability and integrity, due to the detachment of pericytes and leaking junctions between ECs, favored by the interaction between the very late antigen-4 (VLA-4) integrin on cancer cells and vascular cell adhesion protein 1 (VCAM-1) on ECs[12,13] (Fig. 1a). Importantly, the morphological, phenotypical and functional abnormalities of vessels promote EC energy and, through a high grade of intratumoral hypoxia as well as the production of soluble mediators, severely affect transmigration of immune cells to the tumor site. Therefore, the tumor mass becomes restricted to effector immune cells, such as CD8+ cytotoxic T cells, but accessible to immunosuppressive cells, including myeloid-derived suppressor cells (MDSCs), regulatory T cells (Treg) and M2-tumor macrophages (M2-TAM). These latter are in turn stimulated to release mediators, such as VEGF, TGF-β and IL-10, as well as to increase the expression of the immune checkpoint molecules, such as programmed cell death protein 1 (PD-1), T-cell immunoglobulin and mucin-domain containing-3 (TIM-3) and cytotoxic T-lymphocyte antigen 4 (CTLA-4), further powering intratumor immunosuppression and functional inhibition of cytotoxic T cells.[14] In such a scenario, cancer cells, exploiting their functional capabilities to generate a tumor-promoting microenvironment, increase their invasive properties and metastasize outside the three-dimensional (3D) structure of the tumor mass, also favored by peripheral immune tolerance.[15]

Crucial to cancer development is the so-called "immune contexture", defining the nature and the function of the tumor immune content. The generation of a heterogeneous microenvironment within tumor is particularly important for the distribution of infiltrated immune cells, which is not uniform and acquires a different prognostic relevance.[16] Tumors can be classified as hot and cold tumors, mainly according to the type, number, distribution and function of cytotoxic T cells within the tumor mass. Hot tumors are distinguished by in place antitumor immune response associated with the high frequency of functional T cells spatially distributed inside the tumor bed. Conversely, cold tumors, also classified as excluded or immunosuppressed altered tumors, display an immunosuppressive TME with physical exclusion or accumulation of T cell infiltration only

at the tumor edges, leading to incapability to mount the antitumor immune response, as well as to tumor escape and resistance to therapy.[17] In this scenario, dysfunctional tumor vessels may limit optimal drug delivery, and also tumor structural heterogeneity may cause the formation of specific niches with limited physical access to drugs, promoting the survival and self-renewal of cancer stem cells. Accordingly, therapeutic approaches, aiming at normalizing vascular beds within the tumor mass, have been reported to increase the penetration of therapeutic molecules into the tumor and enhance the clinical efficacy of combined treatments.[18] Nevertheless, anti-angiogenic agents, such as bevacizumab targeting the VEGFA pathway, despite their efficacy in disease stabilization, may favor tumor resistance with high patient relapse rates, due to the increase of some variables associated with vascular regression, such as high intratumoral hypoxia and blood flow reduction.[19] In light of this, the immune contexture and vascular dynamics represent key components of the TME that may critically determine both inherent and acquired resistance, not only to immunotherapies but also to other therapeutic agents, thus driving clinical outcomes. For instance, in breast cancer patients undergoing chemotherapy the acquisition of resistance may be associated with the high frequency of macrophages and CD4^{+} T cells along with low levels of CD8^{+} T cells.[20] Conversely, predominant stromal infiltration of the PD-1^{hi}CD8^{+} T subset in triple-negative breast cancer (TNBC) patients was found to define the 'hot' immune status with favorable outcomes associated with improved survival.[21]

Therefore, harnessing the antitumor immunity by immune targeting has become a powerful therapeutic tool. In the last few years, new efficacious immunotherapeutic strategies have been discovered to fight cancer, totally changing the outcome of many types of metastatic cancers, previously considered incurable. In this line, the recent approval of several immunomodulatory agents such as ICIs has revolutionized the therapeutic treatment of many cancers with unexpected clinical benefit.[22] Ipilimumab, the first approved FDA (U.S. Food and Drug Administration) monoclonal antibody targeting the negative immune checkpoint protein CTLA-4, allows enhanced T cell activation while leading to depletion of Treg cells in the tumor bed. Preclinical data, showing the central role of the PD-1/PD-L1 axis in the suppression of effector T cell function, opened the FDA approval to nivolumab and pembrolizumab, both monoclonal antibodies to PD-1, in the treatment of diverse solid cancers, including melanoma, non-small cell lung cancer (NSCLC) and renal cell carcinoma (Fig. 1). In clinical trials, these immunotherapeutic treatments have shown unexpected clear-cut superiority over traditional chemotherapy by restoring T cell activation within the tumor mass.[23] In the same line, other immunotherapeutic approaches have been developed or implemented. Adoptive cell transfer, mainly genetically modified T cells expressing chimeric antigen receptors (CAR T-cells), fosters direct recognition and elimination of cancer cells,[23] whereas dendritic cell-based vaccinations aim at boosting the patient's anticancer immunity by stimulating antigen-specific CD8^{+} T
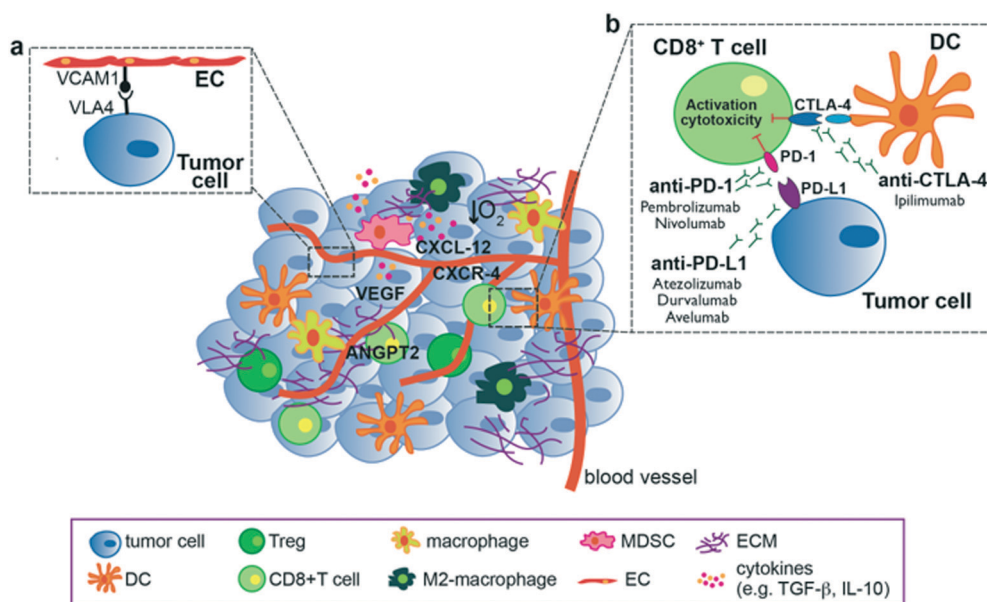

Fig. 1 The landscape of immune–tumor cell interactions within the TME. The TME consists of a heterogeneous population of cancer cells and a variety of resident and infiltrating immune cells along with secreted factors and the ECM. The dynamic cross-talk between microenvironment components and cancer cells drives tumor progression. The interactions between ECs and cancer cells are particularly relevant to metastasis (panel a). Inhibitory immune molecules are key targets for immunotherapeutic interventions such as ICIs (panel b). DCs, dendritic cells; Treg, regulatory T cells; M2-macrophage, M2-tumor associated macrophages; MSCs, mesenchymal stem cells; MDSCs, myeloid–derived suppressor cells; ECM, extracellular matrix.

A Cell-cell interactions
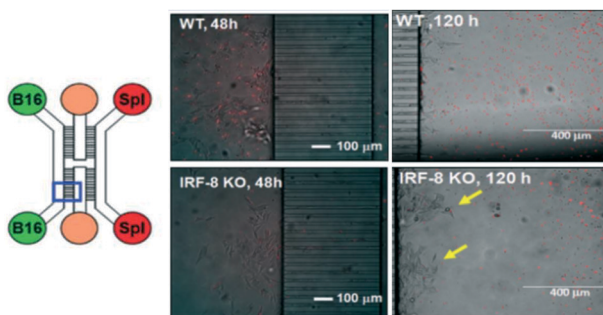
B Functional response to drug treatment
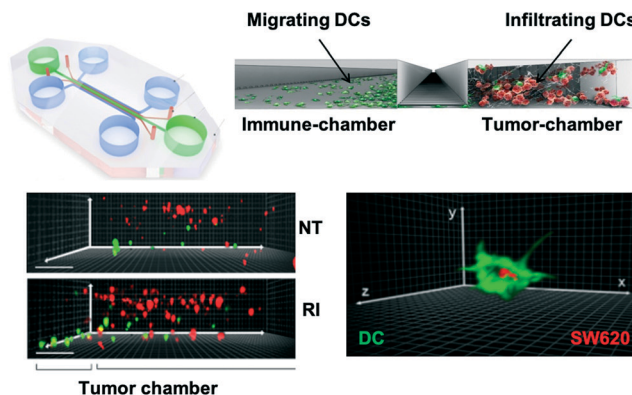
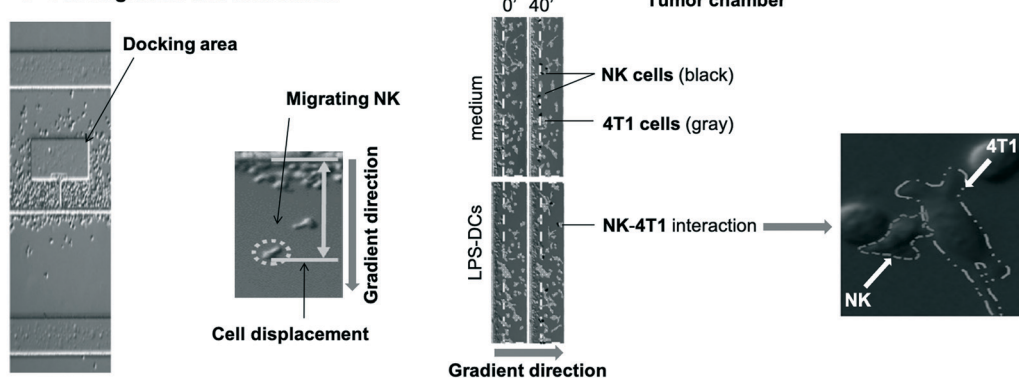## C Cell migration and interaction

Fig. 2 Microfluidic platforms to assess tumor–immune cell interactions and cell migration. (A) The 3D microfluidic platform allows real-time investigation of interactions of adherent cancer cells and floating immune cells. The insets show fluorescence microphotographs of the different migration rates of red-labelled WT and IRF-8 KO murine spleen cells in the melanoma compartment at 48 h, and the preferential extravasation of tumor cells (yellow arrows) seeded with IRF-8 KO spleen cells, after 120 h. Reproduced from ref. 50 with permission from the Royal Society of Chemistry. (B) The 3D microfluidic platform is composed of a central immune chamber (green) connected to side tumor chambers (red) by tight microchannels (upper left panel). 3D graphic rendering of a device section reproducing the movement of DCs (IFN-DCs) from the immune chamber towards the tumor chamber, through the connecting channels (upper right panel). 3D confocal image stacks showing the preferential migration of green-stained DCs towards red-stained drug (RI)-treated cancer cells (SW620) (lower left panels), and the phagocytosis of a red-stained RI-treated cancer cell by a green-labelled DC (lower right panel). Reproduced from ref. 51 (https://creativecommons.org/). (C) NK cell recruitment towards a chemotactic gradient and antitumor activity are assessed by a triple docking device (D³-chip) in which three independent units are equipped with cell docking structures ensuring the alignment of NK cells before starting migration. NK alignment and the analysis of migration displacement of a single NK cell are shown in the left panels. Microscopy images showing the preferential migration of NK cells (black) towards 4T1 breast cancer cells (gray) upon stimulation with conditioned medium from LPS-activated DCs (middle panel). The interaction between one NK cell and one 4T1 cell is shown in the right panel. Adapted and reproduced from ref. 52 (copyright© 2020 Elsevier Inc.).

cells.[24] While most of the current immunotherapeutic approaches, such as monotherapy, have durable responses only in some tumor types and in a limited number of patients, their combination with conventional drugs is under investigation to extend antitumor efficacy as much as possible to all patients and cancer types.[25] In such a scenario, understanding immune–cancer as well as immune–vascular crosstalk within the TME is essential for the development of successful cancer immunotherapies.[26] In this light, the convergence of 3D cell models and microfabrication, leading to patient-derived microfluidic platforms, offers a powerful tool to predict individual responses to immunotherapy.[27,28]

The TME is a complex entity, where the vascular system supports the interaction between a large number of immune components and tumor, which is substantially able to alter its microenvironment. Recreating these intertwined interactions as much as possible in a model is a challenge that

researchers are lately trying to address.[4] Therefore, the reconstitution of tumor heterogeneity, in terms of interactions between different cell populations in a 3D spatial structure, represents an ideal experimental model to test the effects of the TME components on T cell infiltration and, in turn, to study the efficacy of anticancer immunotherapy.[29] Importantly, while traditional two-dimensional (2D) culture models, which offer a valid approach to reproduce limited TME characteristics, are not faithful in terms of complexity and spatial organization,[30] 3D microfluidic tumor models have great potential to recreate the TME complexity.[31] Microfluidic devices are platforms displaying different micrometric geometries, mainly consisting of channels and chambers hosting small amounts of fluids that can support micro-cultures of cells or tissues, allowing the investigation of physio-pathological systems in a highly controlled way. In this line, microfluidics has been exploited to mimic the 3D TME

structure by immune–cancer cell co-cultures into multiple interconnected channels and/or chambers perfused with medium flow under a tight control by integrated valves, filters and programmable pumps, able to regulate crucial parameters like the shear stress, thus strengthening the similarity to the TME.[32–34]

Box 1: Immunotherapy

Immune contexture

It indicates the spatial organization and density of the immune infiltrate in the TME.

Hot and cold tumors

Hot tumors are infiltrated by T cells and exhibit activation of inflammation signals. Cold tumors or non-inflamed tumors lack infiltrating T cells and inflammation signals.

Immunotherapy

Immunotherapy is a biological therapy for cancer treatment supporting the immune system to fight cancer. It is based on molecules, often monoclonal antibodies, mAbs or cells, such as CAR-T cells, produced by the body or modified in a laboratory to improve the capability of the immune system to destroy cancer cells. There are several types of immunotherapy: immune checkpoint inhibitors (ICIs); chimeric antigen receptor (CAR) T-cells; cytokines and immunomodulators; monoclonal antibodies (mAbs); cancer vaccines; oncolytic viruses.

Immune checkpoint inhibitors (ICIs)

ICIs are mAbs targeting immune checkpoints (ICs), which are molecules on certain immune cells with the function of being activated (or inactivated) to start an immune response. Since cancer cells can use ICs to silence the antitumor immune response, ICIs are used to take the "brakes" off the immune system.

Adoptive cell therapy (ACT)

ACT is based on the administration of lymphocytes to cancer patients to activate anticancer response. In autologous cancer immune therapy, patient-derived $CD8^+$ T cells are genetically manipulated to express T cell receptors (TCR) or chimeric antigen receptor (CAR) and then reinfused into patients. NK, DCs, and $CD4^+$ T cells are also used for ACT.

Precision medicine

Precision medicine (PM) is a medical approach for disease treatment or prevention tailored to the individual patient, taking into account individual variability in genetics and other biological and lifestyle characteristics. PM allows the best possible medical treatment to be chosen for a particular disease for each patient instead of the one-size-fits-all approach developed for the average person.

---

3 Designing microfluidic chips for immunotherapeutic studies

With few exceptions, microfluidic chips are fabricated using standard soft lithography, a method that combines the strong potential of photolithography resolution with rapid prototyping. This approach is cost-effective, easy to learn, straightforward to apply, and accessible to a wide range of users. Different fabrication methods are qualified as soft lithography, including replica molding which uses a patterned elastomer as a stamp, mold or mask to generate micropatterns and microstructures.[35] Briefly, the microfluidic geometry is printed on a high-resolution mask to be used as a photomask for contact photolithography; the dissolution of the unpolymerized photoresist produces a positive relief on a silicon wafer, which serves as a molding master to obtain a small series of microdevices by replica molding.[36] The stamps are typically fabricated in polydimethylsiloxane (PDMS), an inexpensive polymer, flexible, optically transparent and easy to handle and to bond to other surfaces. This material is particularly suitable for biological applications due to its permeability to gases, impermeability to water and nontoxicity to cells.[37] Nevertheless, PDMS may have drawbacks, such as the absorption of small molecules which can affect cell signaling dynamics or hydrophobicity, whose applicative limits have been overcome by the use of an epoxy negative photoresist, inert to chemical reactions, impermeable and slightly hydrophilic with good adhesion on glass.[38]

Microfluidic devices allow both 2D and 3D cell cultures.[32,39] In the former case, 2D monolayer cultures of different cell types, seeded in separated compartments, are typically used to study cell migration and cell–cell interactions.[40,41] The natural evolution of 2D systems is the realization of 3D models to mimic the spatial architecture of tissues and organs by the integration of a matrix support composed of extracellular matrix proteins, such as collagen or biocompatible polymers, to embed cells growing in a 3D environment.[30] However, this structure is only the basis of a more complex system that, for a faithful reproduction of the TME, should consider other key components, such as the presence of vasculature. In this regard, different vascular structure models have been used, including functional vascular networks grown in scaffolds or matrices, planar endothelial cell monolayers and ECs covering microchannels to generate EC tubes resembling vessels.[30,42,43] In this latter case, ECs are typically seeded into microfluidic channels where a continuous flow-induced shear stress contributes to the reproduction of the capillary physiology of the vascular barrier.[33,44] This structure is particularly crucial for drug delivery studies simulating blood perfusion through a membrane[33,45] and for understanding extravasation of immune cells into the tumor.[5,46] Hence, microfluidic approaches have the potential to reproduce, in a nanoscale size, TME key components that, thanks to the reduced size and to the employment of optically transparent and low auto-fluorescence materials, can be monitored through confocal and fluorescence microscopy. Accordingly, the cellular dynamics can be captured in real-time through on-chip imaging, such as time-lapse recordings, whose processing by image analysis and algorithms ensures a reliable analytic assessment of the cellular processes.

Noteworthily, microfluidic platforms offer a good alternative to animal models. *In vivo* animal testing is inherently limited due to scientific, management and ethical issues. Large animal models, closer to humans, are costly and subject to greater ethical considerations, while relatively cost-effective small animals exhibit significant differences in physiology and pathology compared to humans. Microfluidic devices provide a more rapid, ethically acceptable and cost-effective alternative to animal studies.[47] Hence, these
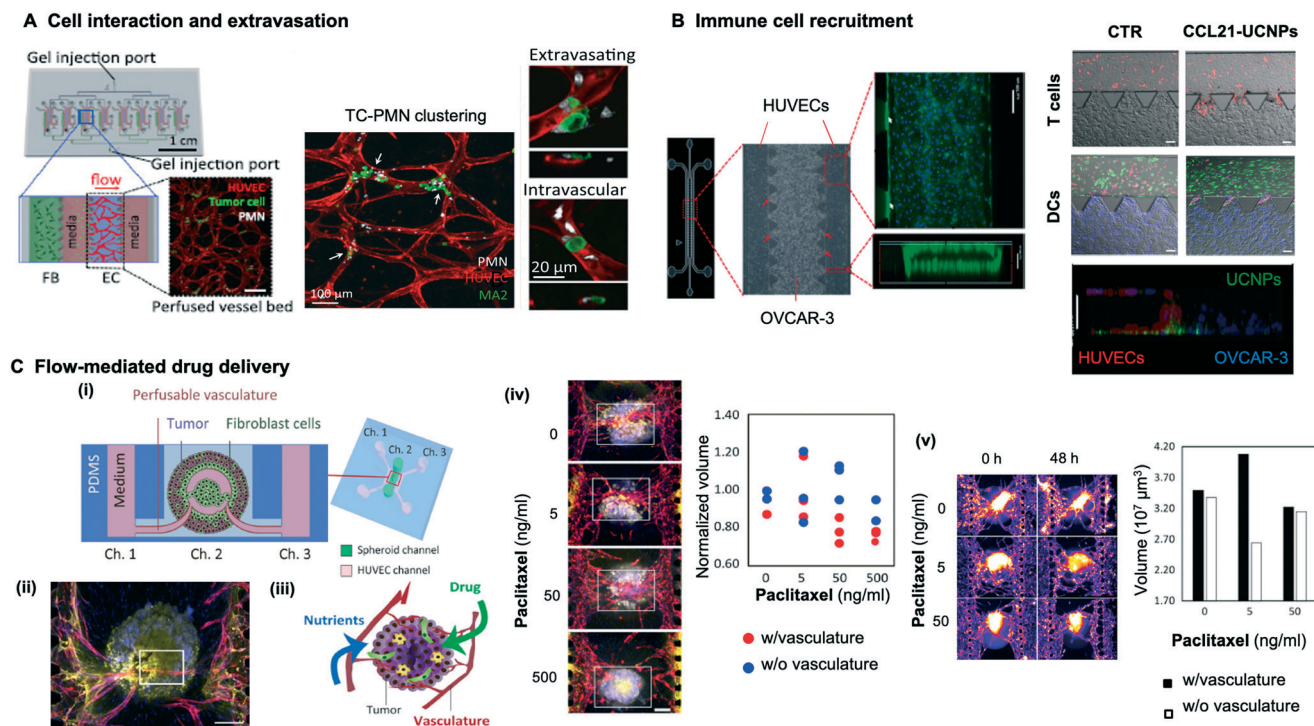
Fig. 3 Functionalization of tumor-on-chips with blood vessels. (A) Microvascular networks are formed in 8 independent hydrogel regions by continuous flow, allowing visualization of tumor–PMN–endothelial interactions and extravasation dynamics (left panel). Confocal image of one vascular network is shown (fluorescence inset); scale bar, 200 μm. Tumor cell–PMN clustering in microvessels results in endothelial barrier disruption and, in turn, tumor cell extravasation (right fluorescence images). Adapted and reproduced from ref. 58 (https://creativecommons.org/). (B) Scheme and bright field image of the microfluidic device with HUVEC and ovarian cancer cell (OVCAR-3) co-culture. Fluorescence images and 3D confocal z-stack rendering showing the 3D vessel structure assembly (scale bar: 100 μm) (left panels). Z-stack analysis showing the entry of nanoparticles (UCNPs) into the tumor cell areas. UCNPs, green; OVCAR-3 cells, blue; HUVECs, red (right lower panel). CCL-21-loaded nanoparticles (CCL21-UCNPs) induce the recruitment of T cells (Jurkat cell line) and DCs into the tumor chamber by crossing the endothelium, as compared to CCL21-unconjugated UCNPs. T cells and DCs, red; cancer cells, blue (DAPI); HUVECs, green (right upper panels). Adapted and reproduced from ref. 59 (copyright© 2019, American Chemical Society). (C) (i) A schematic representation of the PDMS microfluidic device consisting of a central channel loaded with gel-embedded cancer spheroid and lateral channels seeded with HUVECs, able to recapitulate *in vivo* the TME. (ii) Time-lapse recording and fluorescence image analysis allow visualization and quantification of tumor-induced angiogenic sprouts caused by the continuous perfusion of vascular channels. (iii) The recreated vessels enable nutrients and drugs to reach the tumor. (iv) The administration of the chemotherapeutic drug paclitaxel under static conditions leads to a significant reduction of the tumor size, as shown by 2D projection of z-stack images. HUVECs, red; cancer cells (MCF-7), yellow; nuclei, blue. Scale bars: 200 μm. Tumor spheroid volumes are calculated from sequential histological sections. (v) Conversely, paclitaxel administration under perfusion conditions does not induce tumor mass decrease. Scale bars: 200 μm. Adapted and reproduced from ref. 60 (copyright© 2020 Elsevier Inc.).

platforms, allowing the design of complex physiological architectures thus mimicking organs with intrinsic function and physiology, represent one of the most promising techniques for reducing traditional animal testing.[48]

3.1 Tumor-on-a-chip platforms to study cancer–immune cell interactions

Here we reviewed some pivotal studies employing microfluidic platforms to investigate immune–cancer cell interaction with a focus on the cell movement, migratory capability and cell-to-cell interaction.

One of the first attempts employing microfluidic devices to assess immune–cancer cell interactions was done by Huang *et al.*[49] A microfluidic platform was designed to monitor in real time the behavior, upon autocrine and paracrine signals, of metastatic breast cancer cells,

embedded in collagen, and macrophages, seeded in Matrigel, recreating distinct 3D ECM environments. Image analysis demonstrated that macrophages were able to invade only the adjacent channel containing metastatic cancer cells.

A tumor-on-a-chip model devoted to the investigation of immune cell migration towards cancer cells was realized by Businaro *et al.*[50] This PDMS platform was designed for culturing both adherent and floating cell populations and was characterized by a microchannel geometry mimicking the blood vessels that can be actively crossed by cells,; thus it can be considered as a precursor model of microfluidic device for 3D cultures. In fact, the platform held two external cell culture compartments, one loaded with cancer cells and the other with immune cells, connected, *via* four sets of micron-size grooves mimicking the venules, to a central end-closed channel that prevented direct flow of immune cells into the melanoma compartment at the loading time

(Fig. 2A). To mimic the crosstalk occurring between cancer and immune cells within the TME in the presence of diverse immune contexture, splenic immune cells, isolated from wild-type (WT) and interferon regulatory factor 8 (IRF-8) knockout (KO) mice, were co-cultured with melanoma cells and their migration was followed over a week under a microscope. Time-lapse recordings and image analysis[53] demonstrated that IRF-8 deficiency impaired immune cell migration towards cancer cells and their aggregation in clusters, indicating a functional role of IRF-8 against tumor. Interestingly, IRF-8 KO splenic cells were also found to secrete highly tumorigenic soluble factors increasing tumor aggressiveness and empowering melanoma cell motility, thus leading to a major cancer invasion of the immune compartment (Fig. 2A). The same model was upgraded by

Parlato *et al.* to investigate the ability of dendritic cells (DCs) to migrate, in a 3D tumor space, towards tumor cells in response to anticancer treatment.[51] As shown in Fig. 2B the device was composed of five parallel channels. The central one was seeded with human monocyte-derived DCs and was connected, by a series of microchannels, to the two adjacent channels containing human colorectal cancer cells (CRC) embedded in a type I collagen matrix. Two external channels provided nutrients and gas exchange to the tumor channels. CRC cells were treated with a combination of an epigenetic drug, the histone deacetylase inhibitor romidepsin (R), and the immune-modulator cytokine IFN-α (I), reported to induce immunogenic cancer cell death.[54] Time-lapse recording analysis showed that, with respect to untreated cancer, only RI treatment was able to induce a strong DC migration
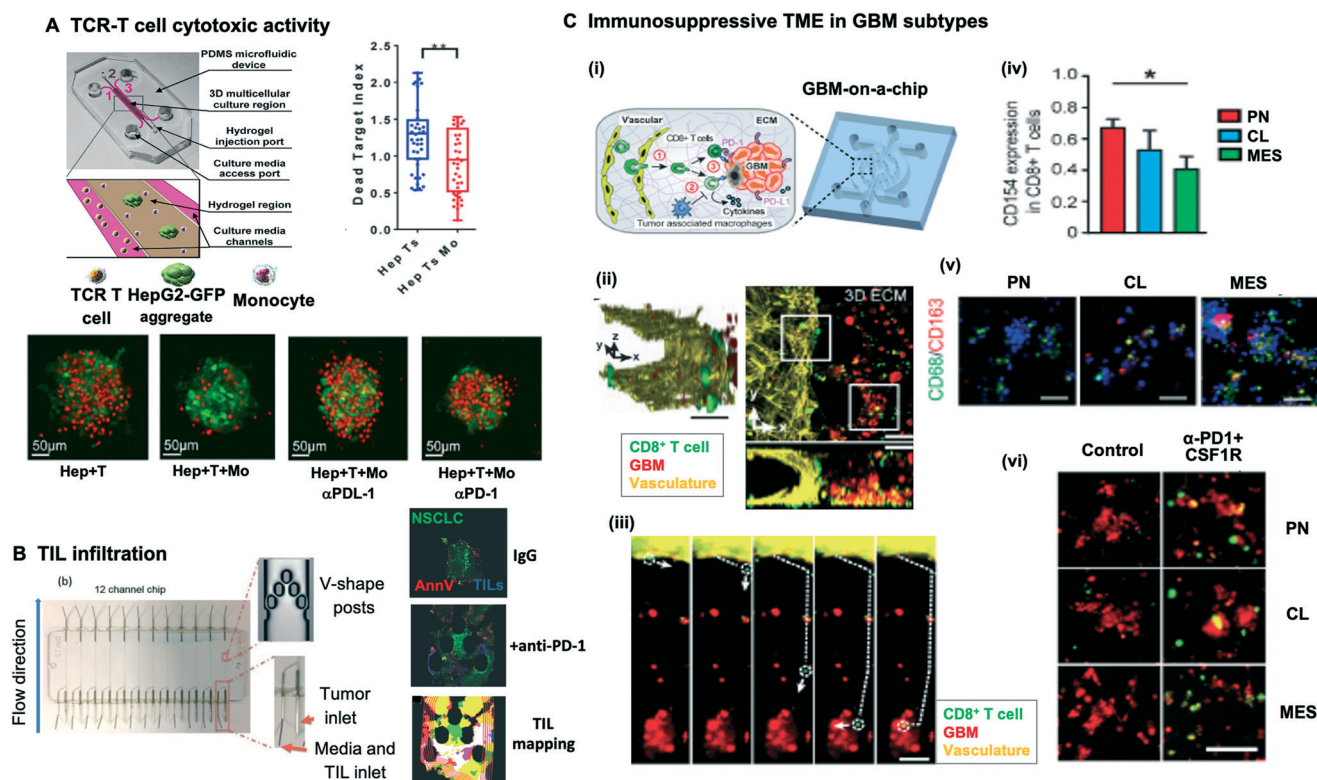

Fig. 4 Microfluidic approaches for testing immunotherapy efficacy. (A) The microfluidic platform holds a central hydrogel region, loaded with human monocytes and target HBV-HCC aggregates, and flanked by two fluidic channels of which one was perfused with HBV-specific TCR T cells (left panel and inset). The inhibitory effect of monocytes on TCR T cells cytotoxic activity is shown in the central box plot. Confocal images showing a GFP-labeled cell aggregate (Hep: green) cultured in the presence of unlabeled HBV-specific TCR T cells (Ts) and monocytes (Mo) with or w/o anti-PDL-1 or anti-PD-1 treatment; target dead cancer cells are in red. Adapted and reproduced from ref. 65 (https://creativecommons.org/). (B) Multiplex microfluidic device with 12 independent channels (left panel): the upper inset shows the tumor V-trapping region in flow stream; the lower inset shows the dual port entry for media and TILs. Confocal images showing the promoting effect of anti-PD-1 treatment on NSCLC tumor killing after 24 hours of TIL perfusion in the presence of isotype control antibody (right upper panel) or anti-PD-1 (right middle panel). Image analytic mapping of time-dependent TIL infiltration is shown (right lower panel): green, tumor cells; blue, TILs; red, dead area; cyan, tumor/TIL overlap; yellow, tumor/dead area overlap; magenta, TIL/dead area overlap; white, tumor/TIL/dead area overlap. Adapted and reproduced from ref. 66 with permission from the Royal Society of Chemistry. (C) (i) TME reconstruction in a GBM-on-a-chip where different GBM subtypes (proneural, PN; classic, CL; mesenchymal, MES) can be analyzed. (ii) 3D reconstruction of a microvessel lumen (yellow) with CD8^{+} T cells (green) and GBM cancer cells (red). Scale bar 50 μm. (iii) Extravasation, ECM infiltration and interaction with GBM cancer cells of a single CD8^{+} T cell analyzed by time-lapse recording. (iv) CD8^{+} T cell activation analysis in PN, CL and MES GBM subtypes by assessing CD154 expression on T cells. Mean intensity is shown. (v) MES subtype shows a more M2-TAM immunosuppressive profile (CD68^{+}/CD163^{+}), compared to PN and CL subtypes. Scale bar, 50 μm. (vi) Enhanced antitumor cytotoxic activity of CD8^{+} T cells by the combined administration of anti-PD-1 antibody and CSF-1R TAM inhibitor. Fluorescence images showing apoptotic (green) and live (red) GBM cancer cells. Adapted and reproduced from ref. 67 (https://creativecommons.org/).

towards and within the 3D TME, *via* CXCR-4/CXCL-12 axis activation. Moreover, confocal microscopy imaging and further cell tracking analysis allowed the identification of phagocytic events and quantification of movement parameters, including the DC velocity and time of interaction of DC–cancer cells (Fig. 2B).

Recently, a triple docking device (D[3]-chip) was employed by Ren *et al.*[52] as a proof-of-concept for monitoring by live-imaging the NK cell migration and their interaction with breast cancer cells. The D[3]-chip consisted of three independent units allowing parallel and independent experiments to be performed. The single units contained a cell docking area to ensure cell alignment before starting migration and had chemical inlets to permit chemoattractant gradient formation (Fig. 2C). The chip structure allowed cells to migrate, through a thin barrier, towards a chemical gradient, thus mimicking the transmigration of cells to inflammatory sites. Briefly, murine 4T1 breast cancer cells were loaded into the outlets, whereas activated NK cells were injected inside the inlets. In each unit, a chemical gradient was generated by means of conditioned medium derived from LPS-activated myeloid DCs (mDCs) or from control medium. Time-lapse recordings and image processing allowed the analysis of cell–cell interaction and cell displacement and tracking of the migration paths (Fig. 2C). Interestingly, activated NK cells exhibited a higher capability to migrate towards and interact with cancer cells in the presence of LPS-activated DCs, suggesting that NK cell recruitment and antitumor activity could be promoted by the occurrence of mature DCs at the tumor site.

Another interesting example of interaction between the tumor and immune system came from the work of Shim *et al.*,[55] reporting a model of *ex vivo* inter-organ communication to recreate tumor-induced immune suppression by cytokine modulation. Slices from tumor-draining (TDLN) and non-draining (NDLN) lymph nodes obtained from breast cancer bearing-mice were separately co-cultured with tumor slices into a dual organ-on-chip. The two culture chambers were interconnected by microchannels and peristaltic pumps and the slices were continuously perfused with unidirectionally recirculating media. Transverse perfusion was ensured by the peculiar culture chamber design that allows the fluid flow to pass through, and not over, the tissue, thus ensuring the diffusion of signalling molecules and mimicking interstitial flow and shear stress. Therefore, the chip design and the circulating flow allowed the depiction of the flow from tumor to lymph nodes and *vice versa*, to observe the reduction of IFN-γ secretion in the TDLN and NDLN with respect to healthy tissue, thus confirming the tumor-induced immunosuppression at both the lymphatic and systemic level. Overall, this modular microfluidic device was suitable to analyze cell migration between tissues, cancer metastasis process and immune cell homing.

3.2 Vascularized tumor-on-a-chip as advanced models to study intercellular interactions within the TME

A key advance for reproducing the TME complexity was the inclusion of the vasculature in the design of tumor-on-a-chip. Particularly worth mentioning in this regard is that many changes of vessel features, such as blood flow, pH, oxygen spreading and morphology, induced by growing tumors, are mostly detected at the level of the capillary network and impact extravasation processes and drug delivery.[56]

Zervantonakis *et al.*[57] developed one of the first platforms able to recreate a 3D tumor–vascular interface. By using high-resolution real-time imaging, they studied the immune-biochemical regulation of cancer intravasation across the endothelium, an important step of the metastatic process. The tumor–vascular interface microfluidic model was designed with three parallel channels, of which two independent channels seeded with tumor and ECs, respectively, were connected by a central 3D ECM hydrogel channel allowing paracrine signaling. Importantly, a hollow vascular lumen was obtained in the endothelial channel generating a 3D ECM–endothelial barrier. Live imaging allowed the investigation of the dynamics of tumor–endothelium interactions and the interplay between cancer cell intravasation and endothelial permeability. When cancer cells were seeded in the 3D matrix, the presence of macrophages in contact with the endothelium induced, *via* a TNF-α-dependent mechanism, a nine-fold increase in cancer cell intravasation.

ECs, as a major cellular component of TME complexity, were investigated by Liu *et al.*[41] through a microfluidic platform designed to study how factors released from vessels could control cell migration within the tumor mass. A PDMS tumor-on-a-chip device, recreating the bladder cancer microenvironment, was built by culturing four different cell populations, namely bladder cancer cells, fibroblasts, macrophages and ECs, in four intersecting cell culture chambers allowing paracrine interactions and cell motility within the TME. The chambers were separated by barriers of hydrogels, which allowed cell communication only through the exchange of soluble factors, nutrients and metabolites as a result of a complex network of microchannels and a perfusion system. Macrophage migration towards cancer cells recorded through optical microscopy was reported as a reliable *in vitro* reconstruction of the monocyte/macrophage recruitment process into the TME. Moreover, this simulation system allowed neo-adjuvant chemotherapy schemes to be tested, thus laying the foundation for individual therapy for bladder cancer.

A high throughput microfluidic chip was exploited in Chen *et al.*[58] using 8 independent hydrogel regions in which self-organized human microvascular networks were loaded with tumor cells for tracking extravasation events by confocal microscopy. A single inlet allowed the simultaneous distribution of cells in the vascular beds *via* a branched microchannel network and the establishment of continuous

flow from an integrated reservoir. Extravasation studies were carried out introducing inflamed polymorphonuclear cells (PMNs), specifically neutrophils, whose role in cancer progression is still a subject of controversy, as they can both hinder cancer progression and promote metastasis in a pro-inflammatory context.[61] Upon inflamed neutrophil and melanoma cell co-perfusion into the vascular channels, neutrophil migration and the formation of tumor cell–PMN aggregates were evaluated by image analysis. Neutrophil spatial localization resulted in endothelial barrier disruption and increased extravasation of adjacent tumor cells (Fig. 3A). Wimalachandra et al.[59] developed a vasculature–tumor interface model by co-culturing ECs and ovarian cancer cells with the final aim of studying the potential of chemokine-functionalized nanoparticles (CCL-21-UCNPs) to enhance the recruitment of T cells and DCs to the tumor site. The microfluidic platform was composed of a central channel, loaded with fibrin-embedded ovarian cancer cells, and two parallel flanking channels seeded with ECs, interconnected via 37 interpost regions. Image analysis showed that the nanoparticles, loaded in the vascular channels, effectively crossed the endothelial barrier and gathered at the tumor–endothelium interface to reach the tumor site. Therefore, chemokine-driven DC and T cell migration from the vascular channel towards the ovarian cancer cells increased, potentially augmenting antitumor immune response (Fig. 3B).

A recent work by Aung et al.[62] employed an improved multicellular tumor-on-a-chip platform to evaluate the influence of some TME components, such as hypoxia and monocytes, on the T cell recruitment into the tumor bed. By using a 3D additive photo patterning approach, breast cancer cells and monocytes were spatially confined within the inner compartment of a bilayer hydrogel, while endothelial cells were loaded within the outer layer, both labeled with fluorescent particles with different emission spectra. The serum medium circulating into the construct created a chemokine gradient, leading to the formation of an endothelial layer at the periphery of the hydrogel construct after 2 days from encapsulation. Cancer breast spheroids were used to reproduce the hypoxia conditions present in the tumor core, while dispersed cancer cells were considered to mimic the tumor periphery, with low levels of hypoxia. The bilayer was then perfused with medium containing activated T cells and their ability to penetrate the construct was evaluated by image analysis, allowing quantification of recruitment and spatial distribution of T cells within the tumor compartment. Notably, cancer spheroids, characterized by elevated hypoxia, recruited a high number of T cells with respect to dispersed cells. Moreover, this process was influenced by the addition of monocytes to the cancer culture and was conditioned by the chemokines secreted into the TME that, in turn, influence the endothelial barrier permeability.

Recently, the development of a tumor-on-a-chip platform mimicking the effects of blood flow on tumors, by incorporation of intraluminal flow in a perfusable vascular network, allowed the evaluation of cancer proliferation and drug efficacy under long-term perfusion conditions.[60] The PDMS device consisted of three channels where tumor spheroids (formed in vitro by human breast cancer, CRC or hepatocarcinoma cell lines), suspended in fibrin–collagen gel, were introduced into the central channel together with lung fibroblasts, whereas HUVECs were loaded into the lateral channels. Time-lapse recording and image analysis allowed the quantification of the area of new tumor-induced angiogenic sprouts in the central channel (Fig. 3C). The continuous perfusion of the vascular network enhanced or maintained the tumor cell activity within the spheroid, in terms of accelerated cell proliferation and survival. Under these conditions, to evaluate the anti-cancer drug efficacy, the chemotherapeutic molecule paclitaxel was administrated under both static and perfusion conditions. In static cultures, the tumor size was found to be dose-dependent on paclitaxel administration, decreasing as the drug dose increased. Conversely, drug administration under perfusion conditions did not induce tumor area and volume decrease (Fig. 3C), highlighting that the inhibition of cellular growth was not drug dose-dependent as observed under static conditions. These results confirmed the relevance to evaluate tumor activities and drug screening in the presence of a vascular network flow.

3.3 Testing immunotherapy by tumor-on-a-chip

In the field of immunotherapy, one of the most important challenges is the possibility to perform preclinical testing of anticancer treatments on microfluidic devices customized with patient-derived cells.[63]

Pavesi et al.[64] employed a previously validated 3D geometry[57] to test the antitumor efficacy of T cell receptor engineered T cells (TCRe-T cells) against antigen-specific hepatocellular carcinoma cells (HCC) confined in a
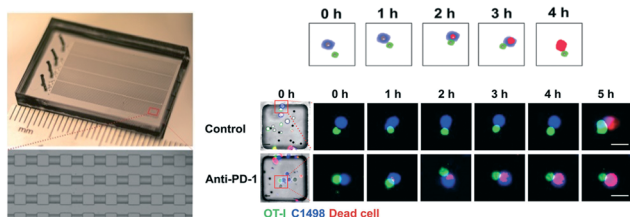

Fig. 5 3D cytotoxicity assays. The microfluidic array composed of more than six thousand wells allows the analysis of, at the single cell level, the immunological synapse between CD8^{+} T cells and leukemia cells. Real-time imaging of CD8^{+} T cells killing activity is shown in the upper insets, where one tumor cell (blue) expresses red fluorescence upon killing by the T cell (green). Real-time fluorescence imaging allows one to observe that the anti-PD-1 treatment accelerates T cell-killing of leukemia cells (lower panels). Adapted and reproduced from ref. 72 with permission from the Royal Society of Chemistry.

microenvironment characterized by hypoxia and inflammation. The device consisted of a central gel channel, loaded with collagen-embedded cancer cells, connected through trapezoidal spacing posts to two side media channels, of which one was filled with fluorescent dye-labelled TCRe-T cells. Real-time live imaging experiments allowed the evaluation of the TCRe-T cells' ability to migrate through the 3D gel matrix and to kill the tumor cells driven by inflammatory cytokines and high oxygen levels. Additionally, this microfluidic device was used to demonstrate that during administration of immunosuppressive drugs, TCRe-T cells retained their cytotoxic antitumor potential, attesting its value in predicting immunotherapy success in defined settings, such as patients undergoing organ transplantation. This microfluidic device was further implemented by Lee et al.[65] to evaluate the antitumor activity of different T cell receptor T (TCR-T) cells engineered to recognize hepatitis B antigen-expressing hepatocellular carcinoma cells (HBV-HCC) in the presence of immunosuppressive monocytes and active PDL-1/PD-1 axis. Collagen-embedded human monocytes and HBV-HCC aggregates, previously cultured to form clusters namely HepG2-preS1-GFP, were injected into the central gel channel to mimic the TME, whereas TCR-T cells were perfused into one of the adjacent fluidic channels (Fig. 4A). Real time analysis of confocal images allowed the detection of the cytotoxic activity of TCR-T cells, crossing the middle 3D gel region, by measuring cancer cell death within HBV-HCC aggregates, showing a strong reduction of cytotoxicity in the presence of monocytes and the full phenomenon reversion by anti PD-L1/PD-1 antibodies (Fig. 4A). Moreover, the 3D TME architectural complexity allowed the determination of the higher cancer lysis activity of engineered TCR-T cells in the outer edge of the tumor mass compared to the core, providing a reliable pre-clinical testing for TCR-T cell therapy efficacy.

To respond to the personalized medicine challenge, Aref et al.[68] employed a commercial microfluidic device to evaluate the response of cancer patients to ICIs, focusing on PD-1 inhibition. Patient-derived organotypic tumor spheroids (PDOTS), retaining autologous tumor-infiltrated PD-1 blockade-sensitive immune cells,[69] were cultured into the center gel region of the 3D microfluidic chamber, separated through a series of posts from the medium/antibody-perfused side channels. Live imaging analysis allowed the detection of fluorescently-labeled immune and cancer cells, and
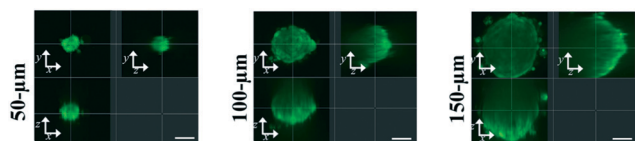
quantification of cellular viability in the presence of anti-CTLA-4 and/or anti-PD-1 antibody, offering the advantage to evaluate dynamic responses to ICIs. A microfluidic model holding patient biopsy-derived tumor fragments was developed by Moore et al.[66] to assess the interactions between tumor and immune cells in a dynamic environment, characterized by continuous perfusion of tumor infiltrating lymphocytes (TILs) or ICI therapies. The microfluidic platform made of a cyclic olefin copolymer comprised a series of parallel and independent channels, designed to accommodate up to 12 different tumor fragments. The channels were aligned in a chevron-like pattern to trap tumor in the central area perfused, by a pressure pump, with medium and TIL flow (Fig. 4B). Each channel was provided with two inlet ports, one for seeding fluorescent green-labeled tumor tissue fragments and the other to introduce, through flow pressurization, red-labeled TILs. Real-time high-resolution imaging along with image analytic algorithms allowed automated and quantitative evaluation of TIL infiltration and tumor death. The efficacy of anti-PD1 therapy, either as pre-treatment of TILs or treatment of human lung tumor fragments after seeding, was also assessed demonstrating the potential of this platform to be applied in a wide range of tumors for pre-clinical testing of emerging ICI combination therapies (Fig. 4B).

A simplified microfluidic device exploiting tumor biopsies for personalized medicine testing was developed by Al Samadi et al.[70] The microfluidic device design, slightly different from that previously described,[50] was composed of a central chamber for the immune cells connected to the neighboring cancer cell-containing channels, filled with a myogel/fibrin matrix. Each chamber of the 3D microfluidic chip was appropriately loaded with freshly isolated red-labelled cancer cells from head and neck squamous cell carcinoma patients, and autologous violet-stained peripheral blood mononuclear cells (PBMCs), in a matrix containing
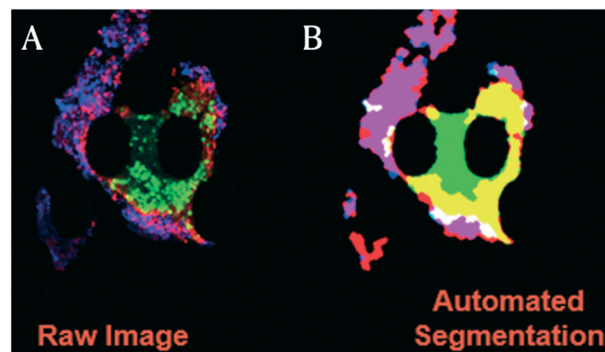

Fig. 6 Fluorescence intensity depth dependence. Fluorescence images of different sized human ovarian granulosa spheroids in the three coordinate planes. Adapted and reproduced from ref. 79 (copyright© 2018, ©SAGE Publications).

Fig. 7 Thresholding-based analysis. (A) Raw confocal microscopy image with the three superimposed channels. False colors correspond to tumor (green), TILs (blue) and apoptotic markers (red). (B) Segmented image identifying different regions. Tumor/TIL overlap is shown in cyan, tumor/dead area overlap in yellow, TIL/dead area overlap in magenta, tumor/TIL/dead area overlap in white. Adapted and reproduced from ref. 66 with permission from the Royal Society of Chemistry.

patient-derived serum, along with anti-PD-L1 antibody or an inhibitor of immunosuppressive indoleamine-pyrrole 2,3-dioxygenase (IDO)-1. By image analysis, the authors showed that, while the IDO-1 inhibitor induced a strong migration of immune cells towards cancer cells limiting cancer cell proliferation, the anti-PD-L1 treatment did not increase this process, thus highlighting the relevance of this microfluidic approach in predicting the efficacy of immunotherapeutic drugs for individual patients.

In another recent report, a novel droplet microfluidic device was used to evaluate immunomodulatory drug activity on 3D tumor–stromal–immune cell spheroids, applying this approach to diffuse large B cell lymphoma (DLBCL).[71] The authors developed, for the first time, a high-throughput method to generate 3D constructs incorporating both lymphoma cells and immune cells (fibroblasts and PBMCs), embedded in a new hydrogel composed of alginate and Puramatrix, a synthetic fiber network very similar to the ECM structure. The device consisted of a droplet docking array with a circular holding site separated by constricted regions. Alginate-embedded cell suspensions were loaded into the device and droplet generation occurred at the T-junction level, followed by multicellular spheroid formation by gelation of the droplets in the docking array by means of calcium chloride. The effect of the continuous perfusion of the anti-cancer drug lenalidomide was assessed, quantifying cell proliferation and cell death by different fluorescent labeling methods of cell populations. The results showed that lenalidomide-induced cancer cell death was enhanced in the presence of activated immune cells and down regulation of pro-inflammatory molecules was observed. This microfluidic approach enabled the generation and assessment of immunogenic tumor spheroids for screening patient-specific immunotherapeutic drugs.

To better understand the limits of anti-PD-1 immunotherapy in glioblastoma (GBM) patients, due to the heterogeneity of immunosuppressive TME, Cui et al.[67] developed a "GBM-on-a-chip" mimicking the different subtypes of GBM tumor niches (proneural, classic and mesenchymal). The chip consisted of a peripheral channel, where human brain microvascular ECs were able to form 3D brain microvessels, an intermediate tumor stromal region, where distinct patient-derived GBM cells were accommodated, and a central area for nutrient supply (Fig. 4C). Allogeneic CD8^{+} T cells from PBMCs were loaded into the 3D brain vessel lumen for monitoring extravasation dynamics and quantifying CD8^{+} T cell migration speed towards tumor cells and tumor infiltration, by means of time-lapse recording and fluorescence image analysis. The interactions between CD8^{+} T cells and in vitro-derived TAMs, as well as with tumor cells, in terms of cytotoxic activity, were analyzed. Results showed a marked reduction of T cell activation and cytotoxic function in all GBM subtypes with respect to the controls, confirming the presence of an immunosuppressive tumor microenvironment. Moreover, the mesenchymal subtype showed a significant increase in immunosuppressive M2-TAMs, compared to the other GBM subtypes. Interestingly, the use of an inhibitor of
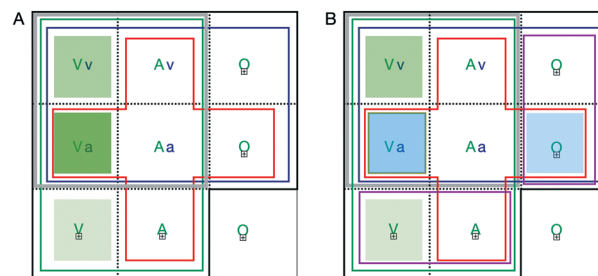

Fig. 8 Cell population partition for viability analysis. (A) Representation of the events involving two types of cells, tumor cells and TILs. Each kind of cell can exist in three states: viable, apoptotic, absent (V/A/O for tumor cells and v/a/o for TILs, respectively). The green contour encloses the subset with tumor cells, whose corresponding event is G. The blue boundary denotes the subset of TILs, b. The red contour represents the set of apoptotic cells of both kinds, symbolized as event α. The gray contour identifies the subset of events where both cell types are simultaneously present. This event is denoted as β. The set is partitioned by the black dotted lines in non-overlapping subsets that completely cover the set. Each subset of the partition is characterized by a state, e.g. V, a, meaning that both types of cells are present, with viable tumor cells (upper case letter) and apoptotic TILs (lower case letter), or O, v, meaning that only viable TILs are present. A probability is attached to each set in the partition, e.g. p(V, a) or p(O, a). Given this information the probability of events that can be constructed by the elementary set operations of union, intersection and of taking complements can be calculated from the axioms of probability. (B) The purple contour (two disjoint components) encloses states with a single type of cell. This event is denoted as γ and is used to estimate the probability that a given apoptotic cell is a TIL.

M2-TAM polarization, combined with the anti-PD-1 treatment, increased CD8^{+} T cell extravasation across microvessels and promoted the cytotoxic functions, with a subsequent increase of tumor cell apoptosis. Moreover, a significant augmentation of TNF-α pro-inflammatory cytokine production and a reduction of the immunosuppressive TGF-β were also observed (Fig. 4C). This ex vivo patient-specific GBM-on-a-chip represented a very interesting tool for testing personalized immunotherapies, identifying new therapeutic biomarkers and improving the long-term patient management.

From the perspective of implementing tumor-on-a-chip for studies aimed at evaluating the efficacy of immunotherapeutic strategies, several studies have been also undertaken to develop 3D cytotoxicity assays on microfluidic devices. Tu et al.[72] designed a microfluidic well array to study T cell cytotoxicity following immune–cancer cell interaction at the single-cell level suitable to dissect the effects of therapeutic treatments on the highly heterogeneous tumor-infiltrating immune population. This platform enabled the evaluation of the time-dependent killing dynamics of CD8^{+} T cells towards leukemia cells in the presence of anti-PD-1 immunotherapy. The PDMS device consisted of an array structure with up to six thousand wells, each one enabling observation of a cell–cell interaction event, built on top of a flow layer, thus forming a wafer with two overlapped layers ensuring a stable cell distribution in the wells (Fig. 5). To perform on-chip T cell cytotoxicity, fluorescently-stained splenic CD8^{+} T cells derived from OT-I mice, genetically

modified to recognize specifically the ovalbumin (OVA), and the OVA-expressing murine leukemia cell line were loaded into the chip at a defined effector–target cell ratio. Real-time imaging analysis by confocal microscopy enabled the evaluation of the killing capability of single T cells in the presence of PD-1 inhibition, confirming the potential of this microfluidic platform for on-chip T cell cytotoxicity testing (Fig. 5). A more complex microfluidic platform was developed by Briones *et al.*[73] to measure granzyme B (GrB) as a cytotoxic effector of immunotherapy efficacy. This study is an interesting proof-of-concept to test the capability of a microfluidic device to detect and measure GrB activity, by using both cellular models, such as GrB-transduced Jurkat T cells and the NK cell line, and primary cells, such as PBMCs isolated from healthy donors, or from anti-PD-1-treated lung cancer patients. The microfluidic device was designed for high throughput parallel monitoring of single cell activity. Compartmentalization of the platform was ensured by two PDMS layers, of which the lower flow layer was designed to mechanically capture single cells by hydrodynamic traps and isolate them in separate micro-chambers sealed by pneumatic valves contained in the upper control layer. In the proof-of-concept experiments for PBMCs, about 110 chambers with trapped single cells were used to measure GrB activity through an enzyme-catalyzed reaction after flushing the chip with a GrB substrate. Confocal microscopy was used to capture and measure the release of the GrB substrate cleaved product and to identify immune cells upon surface marker staining. As expected, the GrB activity was higher in anti-PD-1 treated-lung cancer patient PBMCs with respect to those derived from healthy donors, highlighting the potential of this platform to evaluate the immunotherapy efficacy by the identification of immune effector cells.

4 Algorithms for evaluating cancer–immune cell interactions

Typical algorithms used in studies of on-chip cancer–immune cell interaction elaborate data from digital images coming from different kinds such as bright field, fluorescence and confocal microscopy.[74–77] In the present section, considering few of the recent papers above described, we address basic concepts of image manipulation focusing on a small number of basic algorithms among the most common in the field.

4.1 Image acquisition and digital images

Typically, the hardware collecting the raw data for image acquisition is a microscope[78] with a suitable optical system sending light to a digital camera. The camera is equipped with one or more sensor arrays of $N \times M$ elements, CCD (charge coupled device) or CMOS (complementary metal oxide semiconductor) sensors. The light intensity registered by the sensor is digitized in terms of discrete levels, from the darkest to the lightest, *i.e.* the grey scale. Different channels are usually present in the image acquisition system, such as red, green and blue. Often sequences of images are acquired, *e.g.* in z-stack imaging, where sample slices at different depths are visualized in succession by changing the focal plane or in time-lapse acquisition, where samples are imaged at predefined times.

In fluorescence microscopy, light in a certain wavelength band, selected by optical filters, comes from fluorescent markers used to stain the sample and identify specific cell populations (*e.g.* tumor cells, lymphocytes) and molecules that are indicators of certain processes (*e.g.* cell death). Since fluorochromes possess different excitation and emission bands, they are excited by light sources of appropriate wavelength and their fluorescence light is transmitted/rejected by filters. For a correct image interpretation, it is then crucial to have well separated excitation and emission spectra, which should not overlap among the different fluorochromes to avoid the spillover among channels in a given voxel.[78] Thus, an image pixel registers the signal from the three dimensional volume – voxel – with base corresponding to the imaged area and depth given the slice thickness. Additional complications may arise in analyzing confocal z-stacks of 3D structures, like spheroids, or more geometrically complex objects like tumor fragments, since the detected fluorescence level may be attenuated depending on the local depth of the imaged layer[79] (Fig. 6).
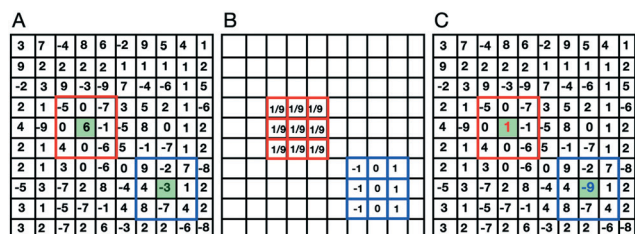
Fig. 9 Mask operations. (A) Original image with superimposed two masks represented by the red and blue square, respectively. (B) The two masks correspond to the operations of averaging (weight 1/9) the image pixels superimposed to the mask (red) and of extracting the horizontal component of the gradient (blue). (C) The effect of the mask operation is to change the value of the image pixel corresponding to the mask center.
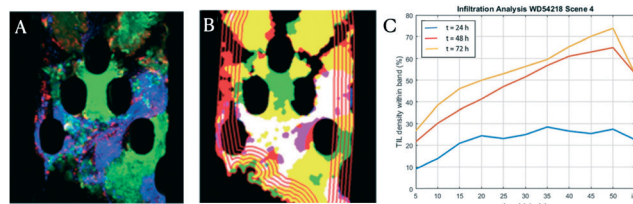
Fig. 10 Distance transform. (A) Raw image of tumor fragment slice. (B) Segmented image showing in red the isolines of the signed distance function (SDF) identifying bands of distance from the tumor border. (C) TIL concentration in the distance bands progressively numbered from the tumor periphery. Adapted and reproduced from ref. 66 with permission from the Royal Society of Chemistry.
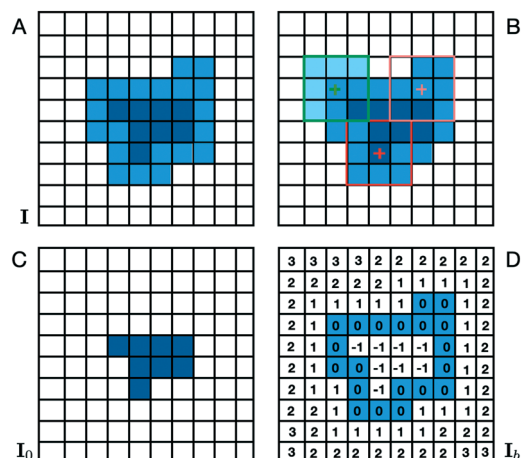
Fig. 11 Morphological operations. (A) A region inside an image. Dark and light blue denote the inner region and boundary of binary image I, respectively. (B) The same image with the superimposed structuring element. Three positions are shown: i) dark red corresponds to the structuring element centered at an interior point, where all pixels of the structuring element belong to the region; ii) the light red and iii) the green structuring elements are centered at a boundary point, where at least one pixel of the structuring element does not belong to the region. (C) The interior part, denoted in blue, corresponds to those pixels for which the structuring element is entirely contained in the original region. A first layer of pixels, those belonging to the boundary, was removed from the region by the erosion process. (D) The boundary, denoted in light blue, is the difference between the region and its interior part. The actual boundary depends on the shape of the structuring element. Both the interior part and boundary would be different if, instead of a 3×3 square, a cross shaped element, defined as a mask with five non-zero, unit weights at $(x - 1, y)$, $(x, y + 1)$, $(x + 1, y)$, $(x, y - 1)$, (x, y) is used. The numbers in each pixel represent the signed distance from the boundary expressed as the (negative of the) number of erosion steps needed to remove the pixel from the region. The square highlighted in green in the top-right panel has three pixels, denoted by the light blue, not belonging to the region. By including all the pixels in the structuring elements as it slides through the region, one layer of pixels is added to the original region. Such a process is called dilation. The newly added layer has distance $d = 1$ from the boundary. Repeating the process from the new configuration, the distance of the added layer from the (original) boundary progressively increases, until a (positive) distance from the boundary is assigned to all pixels (external to the region).

4.2 Preliminary image processing

Suitable algorithms are used to extract the relevant features from the images, such as cell contours, positions and other geometrical factors. Among the available image analysis software packages the most common are ImageJ,[80] Fiji,[81] Metamorph™ and Imaris™. Most of them are developed in user-friendly interfaces amenable to use also by non-specialists of image processing.

Typically, one of the first steps in image manipulation consists of binarization. After defining a threshold intensity intended to separate the signal coming from the relevant features from the background, each pixel is binarized (*i.e.* assigned 0/1 values, with 1 corresponding to white where the signal is above the threshold and 0, black, when it is below). When the threshold is correctly selected, the features of

interest will stand out from the dark background, facilitating further elaboration.

Ideally, since a pixel intensity histogram provides the frequency of level occurrence among the image pixels, the intensity histogram should show two well-distinct peaks, signal and background, respectively. In practice, different forms of noise may affect the image and continuous intensity shades may mask or blur the features. For the analysis of immune cell behavior in tumor-on-a-chip devices, the noise most often comes from the not-removed, non-specific fluorescent material derived from the immunolabelling process or from possible stray light. Under these conditions, the operator selects the threshold based on personal experience. While a large threshold may lose important details, a low threshold may include an undesired background signal producing an effect known as 'flaring'.

Due to the artifacts of an incorrect threshold choice, thresholding has been recently reconsidered. The dependency of the statistical properties of the extracted features on the cut-off is shown to provide guidance in selecting the most appropriate threshold allowing the quantification of the statistical significance of the result.[82]

Prior to binarization, pre-processing of the image may be needed, including procedures such as pixel equalization, noise attenuation (*e.g.* filtering), image enhancement and feature sharpening.

4.2.1 Thresholding-based statistical analysis and algorithmic implementation. A nice illustration of common algorithms is provided by the previously described Moore's work,[66] where segmentation (*i.e.* image feature isolation) is performed by thresholding confocal fluorescence images from z-stack, time-lapse acquisitions of 10 μm slices across whole tumor fragment volumes using combined intensity histogram analysis[83] (Fig. 7). The tumor fragment is hosted in one of the microfluidic channels of the platform in order to study the infiltration of TILs suspended in a stream impinging the fragment with controlled concentration of oxygen, nutrients and tumor sustaining factors, together with a constant supply of the anti-PD-1antibody. Fluorescent markers are used to stain tumor cells (CellTracker Green, green channel), TILs (CellTracker Red, blue channel) and dead cells (Annexin V-APC, as an indicator of apoptosis, red channel).

Tumor viability quantification is here achieved by measuring the ratio of viable to total tumor volume.[66] As explained by the authors, the scenario gets progressively more complicated due to concomitant TIL death. After infiltration, TILs coexist with tumor cells in many voxels, making the red signal non-trivial to be interpreted since two potentially apoptotic populations, tumor and TILs, may be co-located. The tumor viability can be quantified as

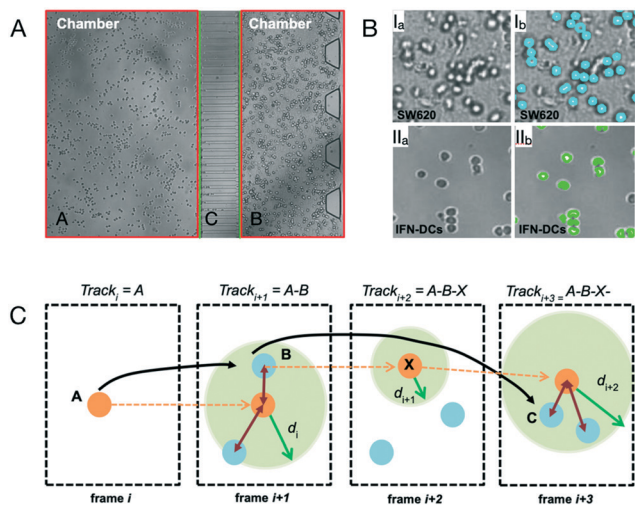$$\mathscr{V} = \frac{p(G, V)}{p(G)} = p(V|G),$$

Fig. 12 Feature extraction and cell tracking. (A) Extraction of background and definition of the image areas corresponding to immune and tumor chambers (red frames, A and B, respectively) and connecting channels (green frame, C). The linear Hough transform is used to extract the rectilinear boundaries. (B) Upper panels show the image segmentation to extract tumor cells (I_a, original image region and, I_b, segmented tumor cells (cyan)). Lower panels show: original image (II_a) and segmented DCs (II_b). (C) Sketch illustrating the algorithm used to link cell positions and to extract cell trajectories. Adapted from the ESI† (http://dx.doi.org/10.1038/s41598-017-01013-x) available for ref. 51 (https://creativecommons.org/).

i.e. the ratio of the joint probability† that a voxel contains viable tumor cells over the probability $p(G)$ that the voxel contains any tumor cell. If only tumor cells underwent apoptosis, the probabilities could be estimated as the ratio of the number of voxels simultaneously associated with the green signal (tumor cells) and no red signal (no apoptosis) over the total number of voxels associated with the green signal. Since part of the red signal may come from voxel with apoptotic TILs and viable tumor, the red channel provides ambiguous information. However, the authors approximately evaluated the probability that an apoptotic cell is a TIL, directly focusing on a subpopulation of voxels containing only TILs, obtaining an estimate of tumor viability as[66]

$$\mathscr{V} \simeq \frac{p(V, o) + p(V, v) + \frac{p(a, \gamma)}{p(\alpha, \gamma)} p(\alpha, \gamma)}{p(G)}.$$

In the above expression, considered that in a voxel each kind of cell can be in three states, such as viable, apoptotic or absent ($V/A/O$ for tumor cells and $v/a/o$ for

† Given two events, V and G, their joint probability $p(G, V)$ is the probability of the two events occurring simultaneously. The conditional probability of V conditioned to G, $p(V|G)$, is the probability of V provided event G occurs. The general relationship between the two probabilities is $p(G, V) = p(V|G)p(G)$.[84] In our case, $p(V|G)$ is the probability that tumor cells are viable in voxels where tumor cells are detected.

TILs, respectively), $p(V, o)$ is the (joint) probability that a voxel contains viable tumor cells and no TILs and $p(V, v)$ is the probability that a voxel contains both viable tumor cells and viable TILs (Fig. 8). The term $p(a, \gamma)p(\alpha, \gamma)/p(\alpha, \beta)$ is the estimated probability that the tumor is viable in voxels containing both kinds of cells of which at least one kind is apoptotic, according to the following symbols: γ is the event of having a single type of cell in the voxel, *i.e.* $p(a, \gamma)$ is the probability of having a voxel with a single type of cell which is an apoptotic TIL; α denotes the event corresponding to apoptosis, *i.e.* $p(\alpha, \gamma)$ is the probability to have a voxel with a single type of cell which is apoptotic (could be either a tumor cell or a TIL); β is the event of having the two kinds of cells co-located in the voxel, *i.e.* $p(\alpha, \beta)$ is the probability of having both kinds of cells in the voxel, at least one of which is apoptotic. The sum of the three terms in the numerator of the expression for the tumor viability provides the estimate for $p(G, V)$.

This analysis can be directly implemented in an image analysis algorithm.[66] In order to achieve this objective, the following operations need to be performed: 1) the product of two images, defined as the image containing the products of corresponding pixel values, *i.e.* $K = I \& J$; 2) the negation of a (thresholded) image, $J = \text{not } I$, where ones are changed to zeroes and zeroes to ones; 3) the scalar product of two images, $s = I \cdot J$, which is the sum of the products of corresponding pixel values to produce a number (the standard scalar product of the corresponding arrays). This operation counts the number of pixels which are simultaneously 1 in both images.

After denoting by **G**, **B** and **R** the thresholded images from the green, blue and red channel, respectively, as previously described in Fig. 7, the probability $p(G)$ that a voxel contains tumor cells is proportional to the number N_0 of pixels in image **G** with value 1, *i.e.* to the sum of the pixel values in the (thresholded) green channel image,

$$p(G) \propto N_0 = \mathbf{G} \circ \mathbf{G} = |\mathbf{G}|.$$

The probability $p(V, o) + p(V, v)$ of viable tumor cells in voxels with no apoptotic cells is proportional to N_1, the number of non-zero pixels in the product image **G** and not **R**, which are 1 at pixels where **G** is 1 and **R** is 0,

$$p(V, o) + p(V, v) \propto N_1 = |\mathbf{G} \& \text{not } \mathbf{R}|.$$

Analogously, the probability $p(\alpha, \beta)$ of having both types of cells in the voxel with at least one apoptotic one is

$$p(\alpha, \beta) \propto N_2 = |\mathbf{G} \& \mathbf{B} \& \mathbf{R}|,$$

being the sum of pixel products of the three thresholded images from green, blue and red channels (all three signals must be present). Finally the probability of apoptotic TILs in voxels with a single type of cell is proportional to the number

of non-zero pixels in the product of images **B** (TILs), **R** (apoptotic cells) and the negation of **G** (tumor cells must not be present, since only one type of cell is allowed),

$$p(a, \gamma) \propto |\mathbf{B} \ \& \ \mathbf{R} \ \& \ \mathrm{Not} \ \mathbf{G}|.$$

Considered the probability $p(\alpha, \gamma)$ of having apoptotic cells in the pixel sub population with a signal from one kind of cell only,

$$p(\alpha, \gamma) \propto |\mathbf{B} \ \& \ \mathbf{R} \ \& \ \mathrm{Not} \ \mathbf{G}| + |\mathbf{G} \ \& \ \mathbf{R} \ \& \ \mathrm{Not} \ \mathbf{B}|,$$

the estimate of tumor cell viability is eventually obtained as[66]

$$\mathscr{V} = \frac{|\mathbf{G} \ \& \ \mathrm{Not} \ \mathbf{R}| + \dfrac{|\mathbf{B} \ \& \ \mathbf{R} \ \& \ \mathrm{Not} \ \mathbf{G}|}{|\mathbf{B} \ \& \ \mathbf{R} \ \& \ \mathrm{Not} \ \mathbf{G}| + |\mathbf{G} \ \& \ \mathbf{R} \ \& \ \mathrm{Not} \ \mathbf{B}|} |\mathbf{G} \ \& \ \mathbf{B} \ \& \ \mathbf{R}|}{|\mathbf{G}|}.$$

4.3 Mask operations

The notion of a mask is often used in image processing and is a basic tool to design more complex operations like those discussed below. A mask operates locally on pixel intensity i. When centered on a pixel, (x_0, y_0), it identifies its neighborhood $\mathcal{N}(x_0, y_0)$ and restitutes a value v function of the intensity distribution in $\mathcal{N}(x_0, y_0)$ (e.g. a square mask of side 3 pixels involves $n_{\mathrm{mask}} = 9$ pixels, namely $(x_0 + k, y_0 + j)$, $k, j = -1, 0, 1$ and $v = f[i(x_0 - 1, y_0 - 1), i(x_0, y_0 - 1), \ldots, i(x_0 + 1, y_0 + 1)]$). Examples of mask operations are reported in Fig. 9.

Masks allow a number of image operations to be performed. Among the most common, it is worth mentioning the following: 1) a mask can select a region of interest (ROI) by setting to 0 the intensity of pixels not belonging to the mask; 2) it can be used to assign to pixel (x_0, y_0) the local intensity mean (mean filter), $w_{kj} = 1/n_{\mathrm{mask}}$, red mask in Fig. 9; 3) it can be a local median filter which, centered on pixel (x_0, y_0), extracts the n_{mask} intensities from the pixels the mask is superimposed to, ranks them by intensity, finds the median value i_{median} and assigns the median value to the pixel, $i(x_0, y_0) = i_{\mathrm{median}}$; 4) it can locally smooth the intensity, for noise reduction or image blurring to remove small details that are unneeded or would spoil further processing.

An important role of masks is in edge detection. Since the pixel intensity changes sharply in the direction orthogonal to an edge, it can be identified by evaluating the intensity change in nearby pixels. This can be done by using masks that evaluate intensity differences, which correspond to the gradient of the intensity field, see the blue mask in Fig. 9. In this case the mask allows the tagging of pixels that are candidate in belonging to an edge and, in more global terms, to the boundary between regions. Image enhancement, like in unsharp masking, can also be obtained by the use of suitably defined masks.

4.4 Morphological transformations

Morphological transformations[85] may be applied to the image for region identification, removal of uninfluential

details and hole filling as well as for boundary extraction. The algorithms are based on a collection of elementary operations such as erosions and dilations.

The paper by Moore et al.,[66] previously discussed in the context of thresholding, provides a chance to describe two morphological algorithms that the authors exploited to measure the progress of the tumor infiltration process (Fig. 10). After a first step for the identification of the tumor boundary, the tumor fragment can be partitioned in shells (or bands) with progressively increasing distance from the border. Therefore, using the previously described techniques, the number of TILs in each shell can be estimated, leading to the quantification of the overall infiltration process.

4.4.1 Boundary extraction using erosions and distance transform. Like the other morphological procedures, morphological boundary extraction is based on a mask, which in this context is called a structuring element. A 3 pixel × 3 pixel square mask can serve the purpose. Assuming that, after thresholding, image I in Fig. 11 contains a single region identified by pixel values of one against a zero background, the mask is made to slide through the image (i.e. $0 \le x \le N - 1$, $0 \le y \le M - 1$). At pixel (x, y) the sum $\sigma = \sum_{k,j=-1}^{1} i(x+k, y+j)$ is evaluated; considering division between integers, the sum is divided by 9, $i_0 = \mathrm{INT}(\sigma/9)$ (the outcome is 1 if $\sigma = 9$ and 0 if $\sigma < 9$); finally pixel (x, y) is assigned the value i_0. The image I_0 generated in this way is called the erosion of image I. As shown in Fig. 11, the result is a layer of pixels stripped off the original region. The difference between the original and the eroded image, $I_b = I - I_0$, contains zeroes everywhere, except at the stripped pixels, thereby identifying the region boundary.

As already anticipated, upon tumor mass boundary identification, the tumor mass is divided in shells of uniform thickness and given distance from the boundary,[66] Fig. 7. In this case, erosions can be used to determine the interior pixel distance from the boundary. The first erosion removes the pixels of the boundary, with distance $d = 0$, leaving the inner part of the original region. A second erosion applied to the new image strips off a second pixel layer. The distance from the boundary is now $d = -1$, assumed as negative toward the interior. Algorithm iteration will find progressively more distant layers, until the region is emptied. In the example shown in Fig. 11, two iterations completely erode the region, with minimum (signed) distance $d = -1$.

Dilations are the dual operations of erosions. They may be used to assign the boundary distance to outer pixels. Using the same structuring element, successive layers are added by including all pixels of the structuring element centered on any pixel belonging to the region. If the structuring element is centered at (x_0, y_0) within the region, mask pixel $(x, y) = (x_0 + k, y_0 + j)$, $k, j = -1, 0, 1$, is first assigned distance $d = d(x, y) \times i(x, y) + (d(x_0, y_0) + 1) \times (1 - i(x, y))$, where i is the pixel value in the current image. Two cases should be discussed: 1) $i(x, y) = 1$, i.e. the pixel (x, y) belongs to the region. In this case d should maintain the previously assigned value; 2) $i(x, y) = 0$,

i.e. the pixel does not belong to the region. In this case the pixel value should be modified to the value of the mask center pixel (x_0, y_0) incremented by one, since it would belong to the first pixel layer just outside the region. The local pixel value is then updated to $i(x, y) = 1$ thus dilating the original image by one pixel layer. The process can then be reiterated, until all pixels are processed. This algorithm, called the distance transform, is extremely intensive from the computational point of view, but faster implementations known since the late sixties can be used.[86]

This algorithm is used by Moore *et al.*[66] to evaluate TIL infiltration. After the signed distance is determined, the tumor fragment image can be segmented into bands of constant width where TIL-containing pixels can be counted, providing the infiltration profiles along the time-lapse acquisition, as shown in Fig. 10.

4.5 Feature extraction and tracking algorithms

The opportunity to discuss techniques alternative to morphological approaches may be found in two papers by Businaro *et al.* and Parlato *et al.*[50,51] focused on cell motility. Among other tools, the Hough transform is an algorithm for the extraction of lines from an image that may be worth mentioning for its common use. The linear Hough transform is used by Parlato *et al.*[51] to extract the rectilinear edges corresponding to the physical boundaries of different chambers and channels present in the microfluidic device (Fig. 12A). The algorithm can be extended to extract other features, *e.g.* circles as in ref. 51 where the position and size of circularly shaped tumor cells, almost immobile in the extracellular matrix, are identified (Fig. 12B).

At variance with tumor cells, DCs are highly motile and can significantly change shape and size by extending dendrites from the blob-like core. Given the high DC shape variability the Hough transform is unsuitable for their segmentation. For this reason, the multi scale blob detector[87,88] was instead used to successfully segment the blob-like appearance of their core,[51] effectively evaluating DCs' position and characteristic scale in each frame of a time-lapse acquisition. Combining the resulting information, the interactions of DCs and tumor cells were eventually inferred and quantitatively studied by measuring the velocity, directional persistence and region of attraction under different stimuli.

Once the positions of motile cells have been determined in each frame of the time-lapse acquisition, a tracking algorithm may be devised[51] to link the presumed positions of the same object at successive instants (Fig. 12C).

The successive position of an object, *e.g.* a cell, located in frame k at position $\boldsymbol{x}(\mathrm{obj}_k)$ is determined by finding the same kind of object in frame $k + 1$, with minimal distance from $\boldsymbol{x}(\mathrm{obj}_k)$. This procedure is called object linking. For an accurate reconstruction, the sampling rate must be fast enough in comparison with the typical velocity, size and distance between objects. The optimal condition for cell linking is obtained when the images of the moving cell in two successive frames are disjoined and yet the distance traveled between the two frames is less than the typical distance to other cells. The scenario becomes more complicated when several moving objects interact, coalesce or break up, thus requiring an implemented approach.[89]

Once the image processing is completed, physical quantities related to immune–tumor cell interactions may be extracted. These parameters include: i) the trajectory executed by a motile cell of the immune system under given stimuli, either artificial, such as exogenous chemokine gradients established within compartments of the microfluidic chip, or released by tumor cells purposely cultured in the chip; ii) the cell propagation speed, either instantaneous, averaged along the trajectory or conditioned to certain events, such as the proximity to a given (tumor) cell; iii) the persistence of the motion direction of the cell and its level of randomness under different conditions. Overall, this approach provides data for the quantitative evaluation of the interactions occurring between components of the immune system and cancer cells within the TME.

5 Conclusions

Following the unexpected success of ICIs in the treatment of melanoma and lung cancer, previously considered incurable, immunotherapy has rapidly become an important therapeutic option for multiple types of solid cancers. In light of this, vast research and clinical investigation efforts are currently focused on developing novel and more efficacious immunotherapeutic approaches for any given patient. However, some key challenges facing cancer immunotherapy require a crucial advancement in pre-clinical research. Among others, the most relevant short-term objectives are: a) to accelerate the understanding of the complex immune–cancer crosstalk, b) to translate pre-clinical knowledge to humans, and c) to predict efficiently cancer immunotherapy efficacy in a patient-centered basis. These goals can only be reached through the development of optimal preclinical models suitable for studying mechanisms of action driving cancer immunity. In such a scenario, microfluidic platforms designed to build advanced tumor-on-a-chip models are emerging as innovative reliable tools capable of overcoming the drawbacks and shortages of *in vitro* systems and animal models commonly used for investigating human antitumor response.

Microfluidic devices can be engineered for recreating tumor heterogeneity characterized by intertwined physical, biochemical and biological components in a 3D spatial structure, thus reflecting the complex aspects of the TME and offering a unique system for depicting interactions between cancer and the immune system. In a relatively simple and direct way, microfluidic devices allow one to understand tumor-specific immune contexture, meeting the increased awareness that distinct immune compartments and requirements within different tissues drive individual

immune response against cancer. This concept becomes crucial for choosing the right immunotherapeutic approach that a patient could benefit from. So far, much progress has been made in developing useful microfluidic platforms for studying immunotherapy on individual patient basis. These tools offer the possibility to assay the antitumor effects of immunotherapeutic strategies towards a specific patient-derived tumor, allowing the tracking of the movement and the activity of the employed antibody- or cell-based therapy up to the level of cancer and immune cells within the structural complexity of the tumor bed. Nevertheless, further research is needed to improve the similitude of these powerful tools with the complex and dynamic TME entity characterized by multiple cellular and soluble components, whose continuous interactions drive cancer development. The relevance of these technologies is expected to grow even faster in the era of personalized medicine, where autologous cells can be exploited in microfluidic devices for drug testing at the individual patient level.

Conflicts of interest

There are no conflicts to declare.

Acknowledgements

Notes and references

1   J. Galon and D. Bruni, *Immunity*, 2020, **52**, 55–81.
2   A. Boussommier-Calleja, R. Li, M. B. Chen, S. C. Wong and R. D. Kamm, *Trends Cancer*, 2016, **2**, 6–19.
3   K. Ronaldson-Bouchard and G. Vunjak-Novakovic, *Cell Stem Cell*, 2018, **22**, 310–324.
4   L. Wan, C. Neumann and P. LeDuc, *Lab Chip*, 2020, **20**, 873–888.
5   M. Buoncervello, L. Gabriele and E. Toschi, *Int. J. Mol. Sci.*, 2019, **20**, 4320.
6   V. Mohan, A. Das and I. Sagi, *Semin. Cancer Biol.*, 2020, 192–200.
7   M. C. Lloyd, J. J. Cunningham, M. M. Bui, R. J. Gillies, J. S. Brown and R. A. Gatenby, *Cancer Res.*, 2016, **76**, 3136–3144.
8   S. Türkcan, L. Kiru, D. J. Naczynski, L. S. Sasportas and G. Pratx, *Cancer Res.*, 2019, **79**, 410–419.
9   C. Carmona-Fontaine, M. Deforet, L. Akkari, C. B. Thompson, J. A. Joyce and J. B. Xavier, *Proc. Natl. Acad. Sci. U. S. A.*, 2017, **114**, 2934–2939.
10 R. J. Gillies, J. S. Brown, A. R. Anderson and R. A. Gatenby, *Nat. Rev. Cancer*, 2018, **18**, 576–585.
11 D. Aguilar-Cazares, R. Chavez-Dominguez, A. Carlos-Reyes, C. Lopez-Camarillo, O. N. H. de la Cruz and J. S. Lopez-Gonzalez, *Front. Oncol.*, 2019, **9**, 1399.

12 V. Aragon-Sanabria, S. E. Pohler, V. J. Eswar, M. Bierowski, E. W. Gomez and C. Dong, *Sci. Rep.*, 2017, **7**, 45835.
13 N. Reglero-Real, B. Colom, J. V. Bodkin and S. Nourshargh, *Arterioscler., Thromb., Vasc. Biol.*, 2016, **36**, 2048–2057.
14 M. B. Schaaf, A. D. Garg and P. Agostinis, *Cell Death Dis.*, 2018, **9**, 1–14.
15 H. Gonzalez, C. Hagerling and Z. Werb, *Genes Dev.*, 2018, **32**, 1267–1284.
16 A. Kirilovsky, F. Marliot, C. El Sissy, N. Haicheur, J. Galon and F. Pagès, *Int. Immunol.*, 2016, **28**, 373–382.
17 J. Galon and D. Bruni, *Nat. Rev. Drug Discovery*, 2019, **18**, 197–218.
18 J. D. Martin, G. Seano and R. K. Jain, *Annu. Rev. Physiol.*, 2019, **81**, 505–534.
19 Y. Haibe, M. Kreidieh, H. El Hajj, I. Khalifeh, D. Mukherji, S. Temraz and A. Shamseddine, *Front. Oncol.*, 2020, **10**, 221.
20 D. G. DeNardo and B. Ruffell, *Nat. Rev. Immunol.*, 2019, **19**, 369–382.
21 L. Guo, C. Cao, S. Goswami, X. Huang, L. Ma, Y. Guo, B. Yang, T. Li, Y. Chi and X. Zhang, *et al.*, *Clin. Sci.*, 2020, **134**, 711–726.
22 B. A. Wilky, *Immunol. Rev.*, 2019, **290**, 6–23.
23 P. Comoli, C. Chabannon, U. Koehl, F. Lanza, A. Urbano-Ispizua, M. Hudecek, A. Ruggeri, S. Secondino, C. Bonini and P. Pedrazzoli, *Ann. Oncol.*, 2019, **30**, 1740–1750.
24 A. V. Baldin, L. V. Savvateeva, A. V. Bazhin and A. A. Zamyatnin, *Cancers*, 2020, **12**, 590.
25 C. Pan, H. Liu, E. Robins, W. Song, D. Liu, Z. Li and L. Zheng, *J. Hematol. Oncol.*, 2020, **13**, 1–15.
26 Y. Huang, B. Y. Kim, C. K. Chan, S. M. Hahn, I. L. Weissman and W. Jiang, *Nat. Rev. Immunol.*, 2018, **18**, 195–203.
27 L. J. Bray, D. W. Hutmacher and N. Bock, *Front. Bioeng. Biotechnol.*, 2019, **7**, 217.
28 G. Scognamiglio, A. De Chiara, A. Parafioriti, E. Armiraglio, F. Fazioli, M. Gallo, L. Aversa, R. Camerlingo, F. Cacciatore and G. Colella, *et al.*, *Br. J. Cancer*, 2019, **121**, 979–982.
29 V. Kumar and S. Varghese, *Adv. Healthcare Mater.*, 2019, **8**, 1801198.
30 M. Shang, R. H. Soon, C. T. Lim, B. L. Khoo and J. Han, *Lab Chip*, 2019, **19**, 369–386.
31 A. Polini, L. Loretta, A. Barra, Y. S. Zhang, F. Calabi and G. Gigli, *Drug Discovery Today*, 2019, **24**, 517–525.
32 M. Rothbauer, H. Zirath and P. Ertl, *Lab Chip*, 2018, **18**, 249–270.
33 G. Silvani, C. Scognamiglio, D. Caprini, L. Marino, M. Chinappi, G. Sinibaldi, G. Peruzzi, M. F. Kiani and C. M. Casciola, *Small*, 2019, **15**, 1905375.
34 S. Y. Tan, Z. Leung and A. R. Wu, *Small*, 2020, 1905055.
35 R. Sivakumar and N. Y. Lee, *Analyst*, 2020, **145**, 4096–4110.
36 J. R. Anderson, D. T. Chiu, R. J. Jackman, O. Cherniavskaya, J. C. McDonald, H. Wu, S. H. Whitesides and G. M. Whitesides, *Anal. Chem.*, 2000, **72**, 3158–3164.
37 Y. Hwang and R. N. Candler, *Lab Chip*, 2017, **17**, 3948–3959.
38 G. Jenkins, in *Microfluidic Diagnostics*, Springer, 2013, pp. 153–168.

39 A. A. Kizilkurtlu, T. Polat, G. B. Aydin and A. Akpek, *Curr. Pharm. Des.*, 2018, **24**, 5386–5396.

40 N. V. Menon, Y. J. Chuah, B. Cao, M. Lim and Y. Kang, *Biomicrofluidics*, 2014, **8**, 064118.

41 P.-F. Liu, Y.-W. Cao, S.-D. Zhang, Y. Zhao, X.-G. Liu, H.-Q. Shi, K.-Y. Hu, G.-Q. Zhu, B. Ma and H.-T. Niu, *Oncotarget*, 2015, **6**, 37695.

42 M. I. Bogorad, J. DeStefano, J. Karlsson, A. D. Wong, S. Gerecht and P. C. Searson, *Lab Chip*, 2015, **15**, 4242–4255.

43 K. Haase and R. D. Kamm, *Regener. Med.*, 2017, **12**, 285–302.

44 S. P. Deosarkar, B. Prabhakarpandian, B. Wang, J. B. Sheffield, B. Krynska and M. F. Kiani, *PLoS One*, 2015, **10**, 1–21.

45 Y. Tang, F. Soroush, J. B. Sheffield, B. Wang, B. Prabhakarpandian and M. F. Kiani, *Sci. Rep.*, 2017, **7**, 1–14.

46 J. S. Jeon, S. Bersini, M. Gilardi, G. Dubini, J. L. Charest, M. Moretti and R. D. Kamm, *Proc. Natl. Acad. Sci. U. S. A.*, 2015, **112**, 214–219.

47 K. Herrmann, F. Pistollato and M. L. Stephens, *ALTEX*, 2019, **36**, 343–352.

48 H. Kimura, Y. Sakai and T. Fujii, *Drug Metab. Pharmacokinet.*, 2018, **33**, 43–48.

49 C. P. Huang, J. Lu, H. Seon, A. P. Lee, L. A. Flanagan, H.-Y. Kim, A. J. Putnam and N. L. Jeon, *Lab Chip*, 2009, **9**, 1740–1748.

50 L. Businaro, A. De Ninno, G. Schiavoni, V. Lucarini, G. Ciasca, A. Gerardino, F. Belardelli, L. Gabriele and F. Mattei, *Lab Chip*, 2013, **13**, 229–239.

51 S. Parlato, A. De Ninno, R. Molfetta, E. Toschi, D. Salerno, A. Mencattini, G. Romagnoli, A. Fragale, L. Roccazzello and M. Buoncervello, *et al.*, *Sci. Rep.*, 2017, **7**, 1–16.

52 X. Ren, A. Alamri, J. Hipolito, F. Lin and S. K. Kung, in *Methods in Enzymology*, Elsevier, 2020, vol. 631, pp. 357–370.

53 E. Agliari, E. Biselli, A. De Ninno, G. Schiavoni, L. Gabriele, A. Gerardino, F. Mattei, A. Barra and L. Businaro, *Sci. Rep.*, 2014, **4**, 1–15.

54 M. Buoncervello, G. Romagnoli, M. Buccarelli, A. Fragale, E. Toschi, S. Parlato, D. Lucchetti, D. Macchia, M. Spada and I. Canini, *et al.*, *Oncotarget*, 2016, **7**, 26361.

55 S. Shim, M. C. Belanger, A. R. Harris, J. M. Munson and R. R. Pompano, *Lab Chip*, 2019, **19**, 1013–1026.

56 D. Caballero, S. M. Blackburn, M. De Pablo, J. Samitier and L. Albertazzi, *Lab Chip*, 2017, **17**, 3760–3771.

57 I. K. Zervantonakis, S. K. Hughes-Alford, J. L. Charest, J. S. Condeelis, F. B. Gertler and R. D. Kamm, *Proc. Natl. Acad. Sci. U. S. A.*, 2012, **109**, 13515–13520.

58 M. B. Chen, C. Hajal, D. C. Benjamin, C. Yu, H. Azizgolshani, R. O. Hynes and R. D. Kamm, *Proc. Natl. Acad. Sci. U. S. A.*, 2018, **115**, 7022–7027.

59 D. C. Wimalachandra, Y. Li, J. Liu, S. Shikha, J. Zhang, Y.-C. Lim and Y. Zhang, *ACS Appl. Mater. Interfaces*, 2019, **11**, 37513–37523.

60 Y. Nashimoto, R. Okada, S. Hanada, Y. Arima, K. Nishiyama, T. Miura and R. Yokokawa, *Biomaterials*, 2020, **229**, 119547.

61 S. B. Coffelt, M. D. Wellenstein and K. E. de Visser, *Nat. Rev. Cancer*, 2016, **16**, 431.

62 A. Aung, V. Kumar, J. Theprungsirikul, S. K. Davey and S. Varghese, *Cancer Res.*, 2020, **80**, 263–275.

63 W. Sun, Z. Luo, J. Lee, H.-J. Kim, K. Lee, P. Tebon, Y. Feng, M. R. Dokmeci, S. Sengupta and A. Khademhosseini, *Adv. Healthcare Mater.*, 2019, **8**, 1801363.

64 A. Pavesi, A. T. Tan, S. Koh, A. Chia, M. Colombo, E. Antonecchia, C. Miccolis, E. Ceccarello, G. Adriani and M. T. Raimondi, *et al.*, *JCI Insight*, 2017, **2**, 1–18.

65 S. W. L. Lee, G. Adriani, E. Ceccarello, A. Pavesi, A. T. Tan, A. Bertoletti, R. D. Kamm and S. C. Wong, *Front. Immunol.*, 2018, **9**, 416.

66 N. Moore, D. Doty, M. Zielstorff, I. Kariv, L. Moy, A. Gimbel, J. Chevillet, N. Lowry, J. Santos and V. Mott, *et al.*, *Lab Chip*, 2018, **18**, 1844–1858.

67 X. Cui, C. Ma, V. Vasudevaraja, J. Serrano, J. Tong, Y. Peng, M. Delorenzo, G. Shen, J. Frenster and R.-T. T. Morales, *et al.*, *eLife*, 2020, **9**, e52253.

68 A. R. Aref, M. Campisi, E. Ivanova, A. Portell, D. Larios, B. P. Piel, N. Mathur, C. Zhou, R. V. Coakley and A. Bartels, *et al.*, *Lab Chip*, 2018, **18**, 3129–3143.

69 R. W. Jenkins, A. R. Aref, P. H. Lizotte, E. Ivanova, S. Stinson, C. W. Zhou, M. Bowden, J. Deng, H. Liu and D. Miao, *et al.*, *Cancer Discovery*, 2018, **8**, 196–215.

70 A. Al-Samadi, B. Poor, K. Tuomainen, V. Liu, A. Hyytiäinen, I. Suleymanova, K. Mesimaki, T. Wilkman, A. Mäkitie and P. Saavalainen, *et al.*, *Exp. Cell Res.*, 2019, **383**, 111508.

71 P. Sabhachandani, S. Sarkar, S. Mckenney, D. Ravi, A. M. Evens and T. Konry, *J. Controlled Release*, 2019, **295**, 21–30.

72 H. Tu, Z. Wu, Y. Xia, H. Chen, H. Hu, Z. Ding, F. Zhou and S. Guo, *Analyst*, 2020, **145**, 4138–4147.

73 J. C. Briones, W. V. Espulgar, S. Koyama, H. Yoshikawa, J. Park, Y. Naito, A. Kumanogoh, E. Tamiya, H. Takamatsu and M. Saito, *Theranostics*, 2020, **10**, 123.

74 H. Peng, *Bioinformatics*, 2008, **24**, 1827–1836.

75 K. W. Eliceiri, M. R. Berthold, I. G. Goldberg, L. Ibáñez, B. S. Manjunath, M. E. Martone, R. F. Murphy, H. Peng, A. L. Plant and B. Roysam, *et al.*, *Nat. Methods*, 2012, **9**, 697.

76 A. Chessel, *Methods*, 2017, **115**, 110–118.

77 E. T. Arena, C. T. Rueden, M. C. Hiner, S. Wang, M. Yuan and K. W. Eliceiri, *Wiley Interdiscip. Rev. Dev. Biol.*, 2017, **6**, e260.

78 A. J. North, *J. Cell Biol.*, 2006, **172**, 9–18.

79 E. Leary, C. Rhee, B. T. Wilks and J. R. Morgan, *SLAS Technol.*, 2018, **23**, 231–242.

80 C. A. Schneider, W. S. Rasband and K. W. Eliceiri, *Nat. Methods*, 2012, **9**, 671–675.

81 J. Schindelin, I. Arganda-Carreras, E. Frise, V. Kaynig, M. Longair, T. Pietzsch, S. Preibisch, C. Rueden, S. Saalfeld and B. Schmid, *et al.*, *Nat. Methods*, 2012, **9**, 676–682.

82 S. J. Johnson and F. R. Walker, *Sci. Rep.*, 2015, **5**, 1–4.

83 P. L. Rosin, *Pattern Recognit.*, 2001, **34**, 2083–2096.

84 W. Feller, *An introduction to probability theory and its applications*, John Wiley & Sons, 1968, vol. 1.

85 R. Gonzales and R. Woods, *Digital Image Processing*, Prentice Hall, 2008.

86 A. Rosenfeld and J. L. Pfaltz, *Pattern Recognit.*, 1968, **1**, 33–61.

87 T. Lindeberg, *Int. J. Comput. Vis.*, 1998, **30**, 79–116.

88 T. Lindeberg, *J. Math. Imaging Vis.*, 2015, **52**, 3–36.

89 J. Jeong, N. J. Frohberg, E. Zhou, T. Sulchek and P. Qiu, *PLoS One*, 2018, **13**, 1–16.